J. Fluid Mech. (1999), *vol.* 400, *pp.* 295–331. Printed in the United Kingdom

A nonlinear model of flow in meandering submarine and subaerial channels

By JASIM IMRAN[1], GARY PARKER[2] AND CARLOS PIRMEZ[3]

[1]Department of Civil and Environmental Engineering, University of South Carolina, 300 Main Street, Columbia, SC 29208, USA
e-mail: imran@engr.sc.edu

[2]Saint Anthony Falls Laboratory, University of Minnesota, Mississippi River at 3rd Ave SE, Minneapolis, MN 55414, USA

[3]Exxon Production Research Company, Post Office Box 2189, Houston, TX 77252-2189, USA

(Received 20 October 1998 and in revised form 10 July 1999)

A generalized model of flow in meandering subaqueous and subaerial channels is developed. The conservation equations of mass and momentum are depth/layer integrated, normalized, and represented as deviations from a straight base state. This allows the determination of integrable forms which can be solved at both linear and nonlinear levels. The effects of various flow and geometric parameters on the flow dynamics are studied. Although the model is not limited to any specific planform, this study focuses on sine-generated curves. In analysing the flow patterns, the turbidity current of the subaqueous case is simplified to a conservative density flow with water entrainment from above neglected. The subaqueous model thus formally corresponds to a subcritical or only mildly supercritical mud-rich turbidity current. By extension, however the analysis can be applied to a depositional or erosional current carrying sand that is changing only slowly in the streamwise direction. By bringing the subaqueous and subaerial cases into a common form, flow behaviour in the two environments can be compared under similar geometric and boundary conditions. A major difference between the two cases is the degree of superelevation of channel flow around bends, which is modest in the subaerial case but substantial in the subaqueous case. Another difference concerns Coriolis effects: some of the largest subaqueous meandering systems are so large that Coriolis effects can become important. The model is applied to meander bends on the youngest channel in the mid-fan region of the Amazon Fan and a mildly sinuous bend of the North-West Atlantic Mid-Ocean Channel. In the absence of specific data on the turbid flows that created the channel, the model can be used to make inferences about the flow, and in particular the range of values of flow velocity and sediment concentration that would allow the growth and downfan migration of meander bends.

1. Introduction

Meandering is perhaps the most common planform morphology of river channels. Through the years the scientific community has consistently maintained an interest in the study of river meandering. The motivations for such attention range from the challenge of explaining a very complex and beautiful phenomenon in relatively simple terms to practical engineering and environmental concerns (Wicker 1983; Salo *et al.*

1986; Sun, Meakin & Jøssang 1996). Numerical and physical models together with field observations over the past few decades have helped scientists place quantitative bounds on the physical factors that affect river pattern, cross-sectional shape, and temporal and spatial evolution. The cause of subaerial meandering and associated migration in alluvial streams is no longer a subject of speculation; most aspects can be explained adequately by means of linear theories developed from the conservation equations of momentum and mass applied to water and sediment, as described below.

Following the original work of Hickin (1974) and Hickin & Nanson (1975), considerable progress has been made by Ikeda, Parker & Sawai (1981), Parker, Sawai & Ikeda (1982), Parker, Diplas & Akiyama (1983), Parker (1983), Beck, Melfi & Yalamanchili (1983), Parker & Andrews (1986), Howard (1992), Johannesson (1988), Johannesson & Parker (1989), and Parker & Johannesson (1989) in understanding and quantifying the initiation, deformation and migration of meander bends in rivers. The deformation and migration of meander bends was described by relating the bank erosion/deposition rate with a near-bank velocity excess/deficit, which was determined from a linear theory of flow and sediment transport. Such analyses have yielded valuable information regarding the growth and migration of meanders, including estimates of wavelength, amplitude growth rate, and downstream rate of shift. Natural rivers have been found to select meander wavelength so that the locus of high streamwise velocity moves toward the outside of the bend slightly downstream of the bend apex. As a result, meander bends can grow laterally and migrate downchannel simultaneously, as often seen in nature. An analysis based on a linear treatment of flow dynamics and a nonlinear treatment of channel geometry was able to describe the asymmetry characteristic of large river bends (e.g. Parker *et al.* 1983). The treatment was adapted to the prediction of channel migration at engineering time scales (e.g. Parker 1982).

The use of such a mechanistic model has become increasingly popular in simulating the evolution of floodplains by rivers that are nearly straight at the beginning. Such models can evolve complex morphology on their own (e.g. Howard 1992; Sun *et al.* 1996; Stølum 1996). The limitations associated with a linear treatment of flow dynamics, however, pose the question of whether the simulated evolution of a long-term geologic-scale phenomenon may look remarkably realistic but nevertheless may be fundamentally flawed due to the neglect of the nonlinearities in the flow dynamics. The models of Smith & McLean (1984) and Nelson & Smith (1989) retain these nonlinearities in the depth-integrated St. Venant equations in an intrinsic coordinate system. Their pioneering analyses provide the starting point for a consideration of flow nonlinearities herein.

Another term of some importance is the dispersion term associated with redistribution of the streamwise momentum by the secondary current as described later in (2.3). It was found by Johannesson (1988) and Johannesson & Parker (1989) to help resolve a contradiction between the theoretical results of Ikeda *et al.* (1981), Tamai & Ikeuchi (1984), Johannesson (1985), and Blondeaux & Seminara (1985) and the experimental results of Kikkawa, Ikeda & Kitagawa (1976). In the present study the governing equations of flow are solved at both linear and nonlinear levels to determine the importance of the nonlinearities as well as the above mentioned dispersion term as they effect the flow in meander bends.

In fact the largest meandering channels on Earth are not subaerial, but instead are found on submarine fans in the deep ocean. Submarine fans are depositional zones found at or beyond the base of the continental slope. The sedimentation is driven by deposition from submarine debris flows or turbidity currents. The latter, which

are turbulent density underflows obtaining their driving force from sediment held in suspension, are of interest here in that they are thought to be the primary mechanism for the formation and maintenance of discrete channels on submarine fans (Imran, Parker & Katopodes 1998).

Many submarine fans show an intricate pattern of channelized distributaries (Pirmez & Flood 1995). Acoustic images indicate that meandering channels are commonly found on submarine fans. Mud-rich fans such as the Amazon (Damuth *et al.* 1983), Rhône (Droz & Bellaiche 1985), Mississippi (Garrison, Kenyon & Bouma 1982; Weimer 1991), Zaire (Droz *et al.* 1996) and Indus (Clark, Kenyon & Pickering 1992) are coursed by intensely sinuous channels. The sinuosity of submarine channels has been found to be as large as three, with recurving meander loops and occasional cutoffs that strongly resemble those of subaerial rivers (Flood & Damuth 1987; Pirmez 1994; Pirmez & Flood 1995). Detailed bathymetry of part of the Amazon Fan is given in figure 1. Although the present focus is meandering on submarine fans, it is worth noting that meandering submarine canyons analogous to incised subaerial rivers are also common. An example is the incised channels of the Peru–Chile forearc region (Hagen *et al.* 1994). These channels are probably due to erosional turbidity currents.

Most submarine canyons and fans are dormant during periods of interglacial high sea stand such as the one that prevails today. The turbidity currents that form them are activated during periods of low sea stand, when continental sediment is directly supplied to the outer edge of the shelf. This notwithstanding, there are a number of fan and canyon systems that are active under present conditions, including the Canyon system in the Peru-Chile forearc region (Hagen *et al.* 1994) and the Zaire Submarine Fan (Droz *et al.* 1996). In addition to these natural cases, the marine disposal of mine tailings has also been responsible for the formation of small-scale channelized fans (Hay 1987*a*).

The planform characteristics of submarine channels can vary considerably from location to location (e.g. Clark *et al.* 1992). Compilations of measurements of submarine channel characteristics suggest, however, that the planform shapes of submarine and subaerial meanders are often nearly indistinguishable from one another in terms of the ratios of meander wavelength to radius and wavelength to amplitude (Flood & Damuth 1987; Weimer 1991; Clark *et al.* 1992; Pirmez 1994). While the surface planform shape of the submarine case appears to be quite similar to the subaerial case, channel cross-section, including the channel width and overall height and size of channel levees, markedly differ between the two environments. In particular, the submarine case is characterized by channel-bounding levees with heights that are on the order of the channel depth itself, i.e. much higher than those of the subaerial case (e.g. Damuth *et al.* 1988).

The reason for these levees being so high is probably associated with the flow itself. In the case of rivers, the effective density difference, i.e. that between water and the air above, is very large. In the case of turbidity currents, however, the effective density difference between sediment-laden water and the sediment-free water above the interface is much smaller. This small difference should exaggerate the response of the flow interface to both curvature and the Coriolis force, resulting in amplified superelevation as compared to the subaerial case. The acoustic image of a turbid underflow at a bend in Rupert Inlet, British Columbia given in figure 2, showing a very large left–right asymmetry in flow thickness in a subaqueous channel of moderate width, illustrates this effect. The Coriolis force has been found to be essentially negligible in even the largest rivers. For the reason cited above, however,

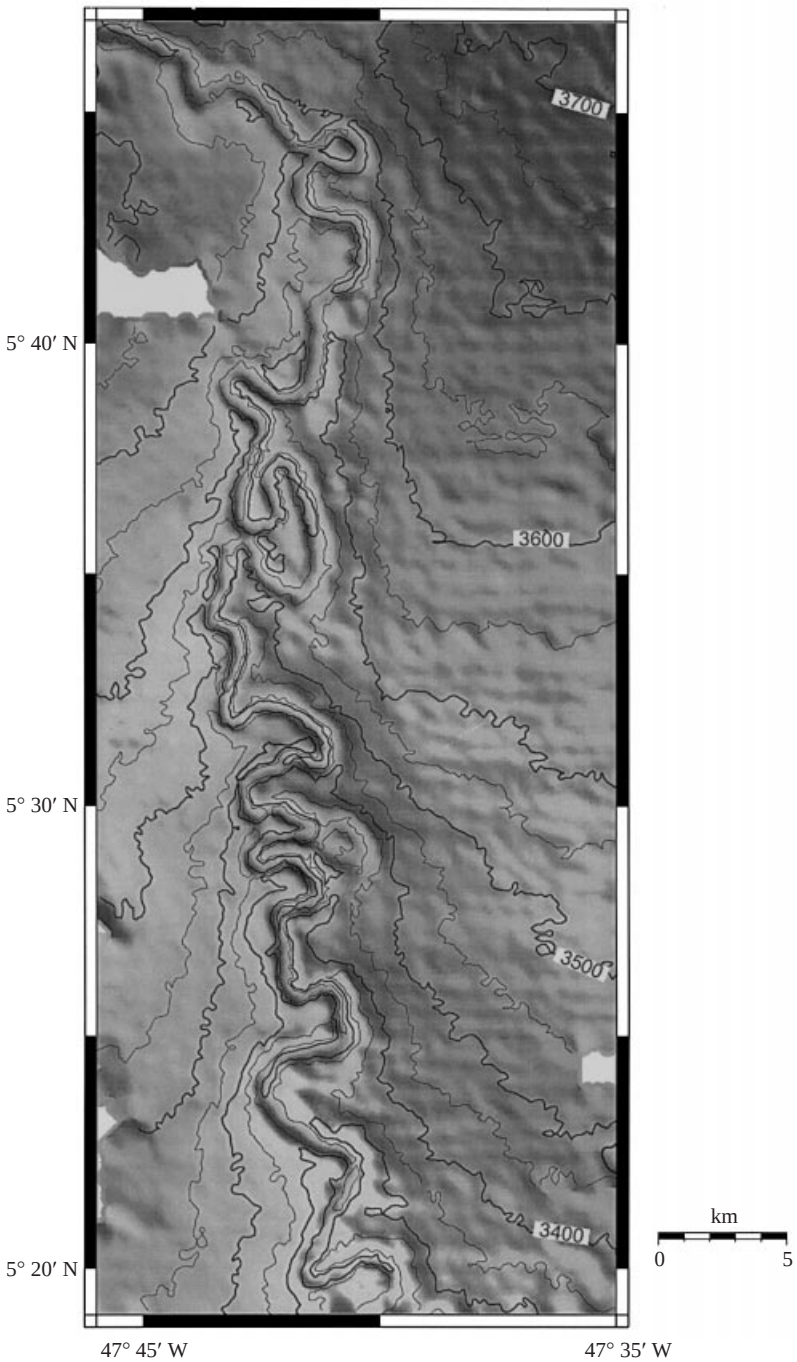

FIGURE 1. Bathymetry of the Amazon Fan near the longitude of 46° W and the latitude of 5° N shows an intricate pattern of channel meandering.

this may not be the case for the turbidity currents that have formed the largest submarine channels (Chough & Hesse 1980). With this in mind the Coriolis force is retained in the present analysis.

The study of subaqueous meandering channels has mostly remained at the level

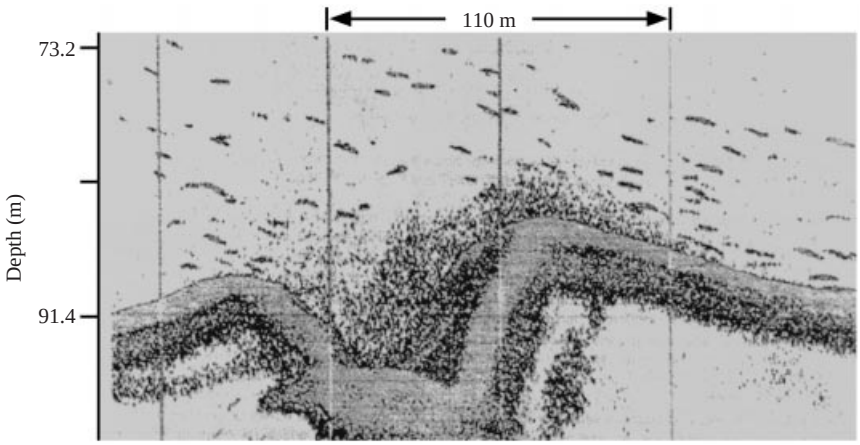

FIGURE 2. Acoustic image of the cross-section of a submarine channel in Prince Rupert Inlet, British Columbia. The higher levee on the right-hand side is associated with the outside of a bend. The image shows an active turbidity current that is so superelevated on the right-hand side that it is spilling over the levee. From Hay (1987*b*), copyright by the American Geophysical Union.

of field observation and interpretation. Unlike river meandering, there have been relatively few attempts to explain the process of submarine channel meandering in terms of the laws of physics. One of the few exceptions is the analysis of Hay (1987*b*). In the present study, an attempt is made to place the study of flow in subaerial and subaqueous meandering channels on an equal footing, so as to be able to compare the two.

2. Theory

Here a simplified meandering channel with constant half-width b and vertical sidewalls is considered. The coordinates are intrinsic with s denoting a centreline downchannel arclength coordinate and n denoting a transverse coordinate normal to s, as defined in figure 3. The channel centreline curvature is defined as

$$C = -\frac{\mathrm{d}\theta}{\mathrm{d}s} \tag{2.1}$$

where θ is the angle of inclination of the channel centreline relative to a straight downvalley coordinate.

The treatment for flow in a meandering river channel is taken directly from the depth-integrated formulation of Johannesson & Parker (1989), but slightly generalized here to include the Coriolis force. The description given here is abbreviated; the reader is referred to that reference and Parker, Fukushima & Pantin (1986) for more details.

2.1. *Flow in a meandering river*

The depth-integrated governing equations for flow in a meandering river are as follows. The relations for the conservation of fluid mass, streamwise momentum and transverse momentum are, respectively

$$\frac{\partial \bar{u}h}{\partial s} + \frac{\partial}{\partial n}[(1 + nC)\bar{v}h] = 0, \tag{2.2}$$

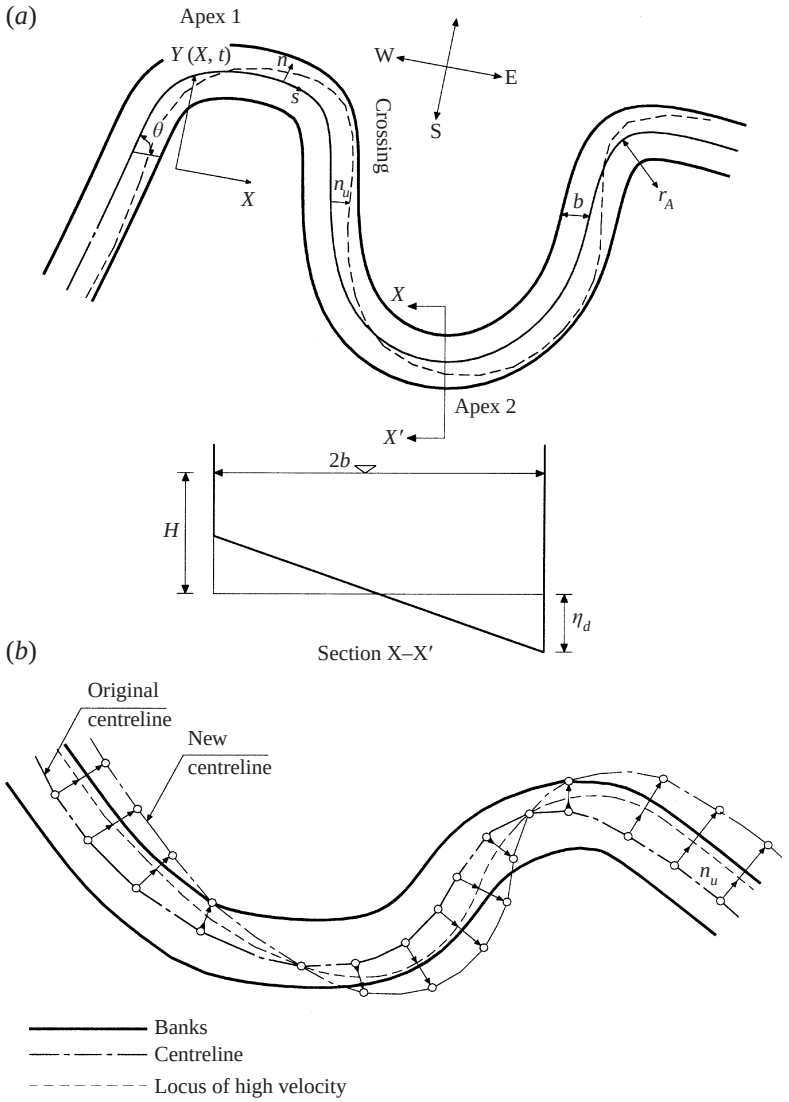

FIGURE 3. (*a*) Definition sketch showing the coordinate system. (*b*) Schematic of meander migration in relation to the locus of high velocity (adapted from Parker 1983 with permission of the ASCE).

$$\frac{1}{1+nC}\bar{u}\frac{\partial \bar{u}}{\partial s}+\bar{v}\frac{\partial \bar{u}}{\partial n}+\frac{C\bar{u}\bar{v}}{1+nC} = -\frac{g}{1+nC}\frac{\partial \xi}{\partial s}-C_f\frac{(\bar{u}^2+\bar{v}^2)^{1/2}}{h}\bar{u}-\frac{1}{h}\frac{\partial}{\partial n}\left(\bar{u}h\overline{T}\bar{v}_s\right)+f\bar{v} \qquad (2.3)$$

and

$$\frac{1}{1+nC}\bar{u}\frac{\partial \bar{v}}{\partial s}+\bar{v}\frac{\partial \bar{v}}{\partial n}-\frac{C\bar{u}^2}{1+nC} = -g\frac{\partial \xi}{\partial n}-C_f\frac{(\bar{u}^2+\bar{v}^2)^{1/2}}{h}\bar{v}-fu. \qquad (2.4)$$

In relations (2.2) to (2.4), $\bar{u}$ and $\bar{v}$ denote depth-integrated fluid velocity in the *s*- and *n*-directions respectively, g is the acceleration due to gravity, C is the channel centreline curvature defined by (2.1), ξ is the water surface elevation, h is the water

depth and C_f is a dimensionless friction factor, considered to be a given constant in the present analysis. In addition, T is a dimensionless shape function averaging to unity which describes to first order the vertical variation of streamwise velocity, and f is the Coriolis parameter, related to the rotational speed of the Earth ω and latitude Φ as follows:

$$f = 2\omega \sin \Phi. \tag{2.5}$$

The parameter v_s is the secondary flow velocity in the transverse direction. The secondary flow in river bends is driven by the local imbalance between the centrifugal force and the transverse pressure force generated by superelevation of the water surface. Here v_s is defined so that it integrates to zero from bed to water surface. The third term on the right-hand side of (2.3) denotes dispersion associated with the redistribution of streamwise momentum by the secondary flow. Several other such dispersion terms are delineated in Johannesson & Parker (1989); these are dropped here since they have been found to be insignificant in previous studies. In the original derivation, the Coriolis force was not considered because it is quite small even for very large rivers. The reason for its inclusion here is to allow comparison between the subaerial and subaqueous environment. It has been found that an integral form of (2.2) is also required to close the problem. Integrating (2.2) between banks, it is found that

$$\int_{-b}^{b} uh \, \mathrm{d}n = Q \tag{2.6}$$

where Q is the total discharge.

2.1.1. *Normalization of the relations*

The following scales are introduced to non-dimensionalize (2.2) to (2.6):

$$\hat{n} = \frac{n}{b},\ \hat{s} = \frac{s}{b},\ \phi = k\hat{s},\ C = \hat{C}/b; \tag{2.7a}$$

$$\hat{u} = \frac{\bar{u}}{U},\ \hat{v} = \frac{\bar{v}}{U},\ \hat{v}_s = \frac{v_s}{U},\ \hat{h} = \frac{h}{H}; \tag{2.7b}$$

$$\xi = \xi_r - Is - H\hat{\xi}_d,\ \eta = \eta_r - Is - H\hat{\eta}_d; \tag{2.7c}$$

$$H = \xi_r - \eta_r,\ f^* = \frac{fb}{U}. \tag{2.7d}$$

In the above U is the equilibrium flow velocity that would prevail in a straight reference channel with the same downstream slope I as the mean slope of the meandering channel measured along the arclength of its centreline. In addition, H is the corresponding reference flow depth, k is a non-dimensional wavenumber related to a characteristic arc wavelength of meandering λ measured along the channel centreline by $k = 2\pi b/\lambda$, ξ_r and η_r are water surface and bed elevation of the reference state at $s = 0$ and $\hat{\xi}_d$ and $\hat{\eta}_d$ are non-dimensional perturbations of water surface and bed elevation respectively. By definition the parameters U, H and I are related as follows:

$$gI = \frac{C_f U^2}{H}, \tag{2.8}$$

i.e. the default form of (2.3) for the reference equilibrium state. The parameter ϕ is a downchannel phase that is incremented by a value of 2π as s is incremented by one characteristic wavelength λ. In addition to the above, the following dimensionless

numbers are introduced:

$$\epsilon = \frac{C_f b}{H} \tag{2.9}$$

and

$$F = \frac{U}{(gH)^{1/2}}. \tag{2.10}$$

Parker & Johannesson (1989) have shown that ϵ is of the order 0.1 and F is of the order of unity in natural channels. The dispersion term in (2.3) was evaluated by Johannesson & Parker (1989) at linear level using an approximate moment method. That evaluation is used here as well to close the problem.

After dropping the hats to avoid clutter, application of an approximation to the transverse momentum equation that is explained and justified in Johannesson & Parker (1989) and some simplification, the non-dimensional equations can be reduced to the following forms:

$$k\frac{\partial uh}{\partial \phi} + \frac{\partial}{\partial n}[(1+nC)vh] = 0, \tag{2.11}$$

$$\frac{k}{1+nC}u\frac{\partial u}{\partial \phi} + v\frac{\partial u}{\partial n} + \frac{Cuv}{1+nC} = \frac{\epsilon}{1+nC} - F^{-2}\frac{k}{1+nC}\frac{\partial \xi_d}{\partial \phi} - \epsilon\frac{(u^2+v^2)^{1/2}}{h}u + \epsilon A_s nC + f^* v, \tag{2.12}$$

$$\frac{Cu^2}{1+nC} = F^{-2}\frac{\partial \xi_d}{\partial n} + f^* u, \tag{2.13}$$

$$\int_{-1}^{1} uh \, \mathrm{d}n = 2, \tag{2.14}$$

where

$$A_s = 181\frac{2\chi^2 + \frac{4}{5}\chi + \frac{1}{15}}{\gamma^2 \chi_1}. \tag{2.15}$$

In (2.15), $\gamma = b/H$, and the terms χ and χ_1 are $O(1)$ dimensionless parameters given by

$$\chi_1 = \frac{C_f^{-1/2}}{13}, \quad \chi = \chi_1 - \tfrac{1}{3}. \tag{2.16}$$

The simplified formulation of the transverse momentum equation precludes the tendency for alternate bars to be damped at large wavenumbers demonstrated by Colombini, Seminara & Tubino (1987).

2.2. *Flow in meandering submarine channels*

Turbidity currents sufficient to create and maintain slowly aggrading channels on submarine fans are likely to be quasi-continuous events. That is, the duration of a channel-forming or channel-maintaining turbidity current is likely to be on the order of many hours or days (e.g. Hay 1987*a*). The layer-averaged equations for the conservation of fluid mass, sediment mass and flow momentum of a continuous

turbidity current containing a uniform grain size can be found in Cartesian form in Imran *et al.* (1998). The treatment allows for variation in time as well as streamwise and transverse directions.

In principle turbidity currents are either erosional or depositional and do not tend to converge toward the normal equilibrium state of rivers (e.g. Parker *et al.* 1986). Submarine fans in particular are depositional environments. This notwithstanding, the fact that many meandering channels on submarine fans extend for hundreds or thousands of kilometres suggests that the downchannel rate of loss of sediment during a channel-maintaining turbidity current may be sufficiently small to allow approximation of the flow as conservative with respect to sediment over several bend wavelengths. This approximation is adopted here for simplicity. In addition, the densimetric Froude number of the turbidity current is assumed to be sufficiently low to allow the neglect of the turbulent entrainment of sediment-free water from above. This latter approximation is strictly valid for turbidity currents that are subcritical or only mildly supercritical in terms of bulk densimetric Froude number. Both of the above mentioned approximations can be relaxed at a later time.

In intrinsic curvilinear coordinates, then, the conservation equations of fluid mass, streamwise momentum and transverse momentum of a quasi-conservative continuous turbidity current within a submarine channel can be respectively expressed as follows:

$$\frac{\partial \bar{u}h}{\partial s} + \frac{\partial}{\partial n}[(1+nC)\bar{v}h] = 0, \tag{2.17}$$

$$\frac{1}{1+nC}\bar{u}\frac{\partial \bar{u}}{\partial s} + \bar{v}\frac{\partial \bar{u}}{\partial n} + \frac{C\bar{u}\bar{v}}{1+nC} = -\frac{Rgc}{1+nC}\frac{\partial \xi}{\partial s} - C_f\frac{(\bar{u}^2+\bar{v}^2)^{1/2}}{h}\bar{u} - \frac{1}{h}\frac{\partial}{\partial n}(\bar{u}h\overline{T}\bar{v}_s) + f\bar{v}, \tag{2.18}$$

and

$$\frac{1}{1+nC}\bar{u}\frac{\partial \bar{v}}{\partial s} + \bar{v}\frac{\partial \bar{v}}{\partial n} - \frac{C\bar{u}^2}{1+nC} = -Rgc\frac{\partial \xi}{\partial n} - C_f\frac{(\bar{u}^2+\bar{v}^2)^{1/2}}{h}\bar{v} - fu. \tag{2.19}$$

In relations (2.17) to (2.19), all the variables are essentially the same as those defined for rivers except for two new ones. These are the submerged specific gravity $R = \rho_s/\rho - 1$ where ρ_s denotes the material density of sediment and ρ denotes the density of sediment-free water, and c, the layer-averaged volume concentration of sediment in the turbidity current column. For natural quartz sediment R has an approximate value of 1.65. Here the turbidity current is assumed to be dilute so that $c \ll 1$. In addition $\bar{u}$ and $\bar{v}$ denote layer-averaged velocities taken over the upward normal direction and h denotes an effective layer thickness of the turbidity current.

In the above equations the concentration c is taken to be constant. Strictly speaking, this assumption applies only to conservative density underflows; here it is assumed that the turbidity current varies sufficiently slowly in the streamwise direction to allow the assumption of constant c over several bends. The default form of the equation of streamwise balance (2.18) for a reference equilibrium flow in a straight channel with slope I now becomes

$$RgcI = \frac{C_f U^2}{H}. \tag{2.20}$$

Equations (2.17), (2.18) and (2.19) can be reduced precisely to the forms of (2.11), (2.12) and (2.13) as well as the integral form of (2.14) using the scalings of (2.7) with

the one exception that the Froude number F must be generalized to the densimetric form

$$F = U/(RgcH)^{1/2} \tag{2.21}$$

where $Rc = 1$ for subaerial flow and $c \ll 1$ for a submarine turbidity current.

A little is known about the convective transport of primary momentum by secondary flow in subaqueous environment, the redistribution term is dropped for simplicity in treating the submarine case. It can be added at a later time. When comparison between rivers and submarine channels is made, this term is set equal to zero in both environments. An additional constraint given by (2.6) applies here as well.

The above analysis allows the treatment of the subaerial and subaqueous cases using a common set of equations. In the next section a procedure is outlined to solve (2.11) to (2.14).

3. Solution procedure

The solution technique outlined here is based on a similar one from Smith & McLean (1984). The form presented here facilitates easy comparison between the linear and nonlinear contributions to the solution. The governing partial differential equations are cast in a way that allows iteration on direct integral forms rather than discretized. The normalized dependent variables in (2.11) to (2.14) can be expressed in the following deviatoric form:

$$u = 1 + u_d, \quad v = 0 + \epsilon v_d, \tag{3.1a,b}$$

where u_d and v_d are deviations about the base state that would prevail in a straight channel with a slope equal to the average centreline slope of the meandering channel. In addition, ξ_d and u_d represent deviations generated by curvature that are further decomposed to the sum of a form that is a function of ϕ only and a form that is a function of both ϕ and n but integrates to zero in the transverse direction; that is

$$\xi_d = \xi_{dc} + \xi_{dd}, \quad \int_{-1}^{1} \xi_{dd}\,\mathrm{d}n = 0, \tag{3.2a}$$

$$u_d = u_{dc} + u_{dd}, \quad \int_{-1}^{1} u_{dd}\,\mathrm{d}n = 0. \tag{3.2b}$$

In (3.1b) the previously defined parameter ϵ appears as a result of the scaling requirement discussed in Johannesson & Parker (1989) that allows the neglect of most terms in the equation of transverse momentum balance.

It is demonstrated in Johannesson & Parker (1989) that for typical meandering streams both the dimensionless wavenumber k and ϵ are of order 0.1, so that the renormalization of k given by

$$r = k/\epsilon \tag{3.3}$$

renders the $O(1)$ parameter r. In addition, deviatoric bed elevation η_d can always be decomposed into the sum of a term η_{dc} varying only with ϕ and a term η_{dd} satisfying

$$\int_{-1}^{1} \eta_{dd}\,\mathrm{d}n = 0. \tag{3.4}$$

In the present analysis flow over a bed of known topograpy is considered. Although

the analysis generalizes for arbitrary forms of η_{dc} and η_{dd} as long as they are not larger than $O(1)$, here η_{dc} is set equal to zero for simplicity.

The expressions (3.1) to (3.3) are substituted into (2.12), (2.11), (2.13), and (2.14); (2.11) is integrated in n subject to the boundary condition of vanishing lateral velocity at the banks and the terms are rearraged to yield the following forms:

$$\begin{aligned} r\frac{\partial}{\partial\phi}(u_{dc}+u_{dd})+(2u_{dc}+2u_{dd}+\eta_d-\xi_{dc}-\xi_{dd}+nC-A_snC) \\ +rF^{-2}\frac{\partial(\xi_{dc}+\xi_{dd})}{\partial\phi}-f^*v_d \\ =1-\frac{(1+nC)(1+u_{dd}+u_{dc})[(1+u_{dd}+u_{dc})^2+\epsilon^2v_d^2]^{1/2}}{1+\xi_{dc}+\xi_{dd}-\eta_d} \\ +(2u_{dd}+2u_{dc}+\eta_d-\xi_{dc}-\xi_{dd}+nC)-Cv_d(1+u_{dc}+u_{dd}) \\ -(u_{dd}+u_{dc})\frac{\partial}{\partial\phi}(u_{dc}+u_{dd})-(1+nC)v_d\frac{\partial u_{dd}}{\partial n}+f^*nCv_d, \end{aligned} \tag{3.5}$$

$$\begin{aligned} v_d+r\frac{\partial}{\partial\phi}\int_{-1}^{n}(u_{dc}+u_{dd}+\xi_{dc}+\xi_{dd}-\eta_d)\,\mathrm{d}n' \\ =-v_d[\xi_{dc}+\xi_{dd}-\eta_d+nC(1+\xi_{dc}+\xi_{dd}-\eta_d)] \\ -r\frac{\partial}{\partial\phi}\int_{-1}^{n}(u_{dc}+u_{dd})(\xi_{dc}+\xi_{dd}-\eta_d)\,\mathrm{d}n', \end{aligned} \tag{3.6}$$

$$F^{-2}\frac{\partial\xi_{dd}}{\partial n}-C+f^*(1+u_{dd}+u_{dc})=C\left[\frac{(1+u_{dc}+u_{dd})^2}{1+nC}-1\right], \tag{3.7}$$

$$\xi_{dc}+u_{dc}=-u_{dc}\xi_{dc}-\frac{1}{2}\int_{-1}^{1}u_{dd}(\xi_{dd}-\eta_d)\,\mathrm{d}n. \tag{3.8}$$

Note that in every case above the fundamentally linear terms have been placed on the left-hand side of the equation and the nonlinear residuals have been placed on the right-hand side. That is, although the equations retain all essential nonlinearities of the flow, the linear formulation is recovered by setting the right-hand side equal to zero.

In order to simplify the notation, the nonlinear residuals on the right-hand side of equations (3.5) to (3.8) are abbreviated to R_1, R_2, R_3 and R_4 respectively. Integration of (3.5) from bank to bank yields

$$r\frac{\partial u_{dc}}{\partial\phi}+2u_{dc}-\xi_{dc}+rF^{-2}\frac{\partial\xi_{dc}}{\partial\phi}=\bar{R}_1 \tag{3.9}$$

where

$$\bar{R}_1=\frac{1}{2}\int_{-1}^{1}R_1\,\mathrm{d}n. \tag{3.10}$$

Subtraction of (3.9) from (3.5) gives

$$r\frac{\partial u_{dd}}{\partial\phi}+2u_{dd}+\eta_d-A_snC-\xi_{dd}+nC+rF^{-2}\frac{\partial\xi_{dd}}{\partial\phi}-f^*v_d=R_1-\bar{R}_1. \tag{3.11}$$

Simplification of (3.6) gives

$$v_d + (n+1)r\frac{\partial}{\partial\phi}(u_{dc} + \xi_{dc}) + r\frac{\partial}{\partial\phi}\int_{-1}^{n}(u_{dd} + \xi_{dd} - \eta_d)\,\mathrm{d}n' = R_2. \tag{3.12}$$

Equations (3.7) and (3.8) can be expressed respectively as

$$\frac{\partial\xi_{dd}}{\partial n} - F^2C + F^2f^*(1 + u_{dd} + u_{dc}) = F^2R_3 \tag{3.13}$$

and

$$\xi_{dc} + u_{dc} = R_4. \tag{3.14}$$

Elimination of u_{dc} from (3.9) using (3.14) yields the following form:

$$\frac{\partial\xi_{dc}}{\partial\phi} - \frac{3F^2}{r(1-F^2)}\xi_{dc} = R_5 \tag{3.15}$$

where

$$R_5 = \frac{F^2}{r(1-F^2)}\left(\bar{R}_1 - 2R_4 - r\frac{\partial R_4}{\partial\phi}\right). \tag{3.16}$$

The analysis up to this point is completely general and can be applied with appropriate boundary conditions. In solving the above, first all the nonlinear residuals are set to zero and a linear solution is obtained. The linear solution is then used to estimate the nonlinear residuals, after which the equations are solved again for an improved solution. The process is repeated until convergence.

Here periodic boundary conditions are assumed for simplicity. That is, any parameter at $\phi + 2\pi$ is set equal to its value at ϕ. If the normalized length of a channel reach is multiple of 2π, then for any variable Γ

$$\Gamma|_{\mathrm{u/s}} = \Gamma|_{\mathrm{d/s}} \tag{3.17}$$

where u/s and d/s denote upstream and downstream respectively.

3.1. *Analytical solution*

Of all the possible shapes for a sinuous channel, perhaps the simplest one is the sine-generated curve. This periodic shape is specified in terms of the angle of inclination of the channel centreline relative to a straight downvalley coordinate as a function of arc distance along channel centreline, as shown in figure 3. Let θ denote this angle; for a sine-generated curve,

$$\theta = \theta_0\cos\phi \tag{3.18}$$

where θ_0 denotes angular amplitude and ϕ is phase, related to arclength distance via (2.7*a*). Here, let C denote channel centreline curvature made dimensionless with half-width b; it follows from (2.1) and (3.18) that

$$C = C_0\sin\phi \tag{3.19}$$

where C_0 denotes the curvature amplitude and is given by

$$C_0 = k\theta_0. \tag{3.20}$$

Rivers with self-formed bends typically form a transverse bed slope such that the bed is lower on the outside and higher on the inside of the bend. This morphology

is commonly known as bar-pool topography. A number of researchers have demonstrated that this transverse bed slope is an increasing function of centreline curvature as long as curvature is not too high (Engelund 1974; Zimmerman & Kennedy 1978; Odgaard 1981; Johannesson 1988). Johannesson & Parker (1989) have developed a theoretical justification for the following very simple but reasonable assumption for channel bed structure:

$$\eta_{dc} = 0, \tag{3.21a}$$

$$\eta_d = \eta_{dd} = -AnC = -C_0 An \sin\phi. \tag{3.21b}$$

In the above relation A is a positive $O(1)$ parameter; a predictive relation for A is given in Johannesson (1988). Where assumptions need to be made here about channel planform and bed topography, the relations (3.19) and (3.21) are utilized. The theory itself, however, is capable of handling much more general planforms and bedforms. Note that (3.21*b*) identically satisfies (3.4).

The specified forms (3.19) and (3.21*b*) for channel curvature and bed profile, respectively, are linear in curvatue amplitude C_0. They serve to introduce forcing terms of order C_0 into governing relations (3.11) to (3.13). The effect of this forcing can be analysed by performing an expansion in C_0, as illustrated in Johannesson & Parker (1989). The linear response can be obtained by dropping the nonlinear residuals, i.e. terms $\sim C_0^2$ and higher in (3.11) to (3.13), and solving the equations subject to cyclic boundary conditions. The nonlinear residuals are strictly negligible in the limit of small curvature, i.e. $C_0 \ll 1$. While it is possible to obtain a solution in closed form with the inclusion of the Coriolis terms, the form is quite cumbersome. With this in mind the analytical solution of the linear problem associated with the neglect of the Coriolis terms is given in the Appendix. The solution is essentially that given in Johannesson & Parker (1989).

Also given in the Appendix are the results of a nonlinear expansion in curvature C_0 of the same problem, carried out to second order, again upon dropping the Coriolis terms. These analytical results are compared with the results of the full numerical scheme given below.

3.2. *Numerical solution at the linear level*

As noted above, it is possible to obtain the linear solution explicitly including the Coriolis terms. The result is so cumbersome that it is easier to bring them into the solution iteratively. To do this all the residual terms R are set equal to zero. It is quickly seen from (3.9) and (3.14) that the only linear solution for ξ_{dc} and u_{dc} is such that both vanish; i.e.

$$\xi_{dc} = 0 \tag{3.22}$$

and

$$u_{dc} = 0. \tag{3.23}$$

Integration of (3.13) in n yields the following:

$$\xi_{dd} = F^2(C - f^*)n - F^2 f^* \int_{-1}^{n} u_{dd}\, \mathrm{d}n' + F_\xi(\phi) \tag{3.24}$$

where $F_\xi(\phi)$ denotes a free function of integration in ϕ. Integration of (3.24) between two banks and use of the fact that ξ_{dd} is defined to integrate to zero between two

banks according to (3.2) gives the following evaluation of $F_\xi(\phi)$:

$$F_\xi(\phi) = \tfrac{1}{2}F^2 f^* \int_{-1}^{1}\int_{-1}^{n} u_{dd}\,\mathrm{d}n'\,\mathrm{d}n''. \tag{3.25}$$

Integration of (3.11) from an upstream point where $\phi = 0$ yields

$$u_{dd} = \mathrm{e}^{-2\phi/r}\left[u_{dd}|_{\mathrm{u/s}} - \frac{1}{r}\int_0^\phi \left(-\xi_{dd} + \eta_d + rF^{-2}\frac{\partial \xi_{dd}}{\partial \phi} + nC - A_s nC - f^* v_d\right)\mathrm{e}^{2\phi/r}\,\mathrm{d}\phi'\right]. \tag{3.26}$$

Applying a periodic boundary condition in u_{dd} to the above equation, it is found that

$$u_{dd}|_{\mathrm{u/s}} = -\frac{1}{r(\mathrm{e}^{2\phi_L/r}-1)}\int_0^{\phi_L}\left(-\xi_{dd} + \eta_d - A_s nC + rF^{-2}\frac{\partial \xi_{dd}}{\partial \phi} + nC - f^* v_d\right)\mathrm{e}^{2\phi/r}\,\mathrm{d}\phi \tag{3.27}$$

where ϕ_L denotes the value of ϕ at the downstream end. Equation (3.12) simplifies to

$$v_d = -r\frac{\partial}{\partial \phi}\int_{-1}^{n}(u_{dd} + \xi_{dd} - \eta_d)\,\mathrm{d}n'. \tag{3.28}$$

To start the solution, u_{dd} and v_d are first set equal to zero. This yields a solution for ξ_{dd} from (3.24), then an evaluation of u_{dd} from (3.26). Once these parameters are known, v_d can be determined from (3.28). The known values of the variables are used to solve (3.24) to (3.28) again until the solution converges. This is typically realized within 2–3 iterations. Here, the numerical integrations are performed using the trapezoidal rule. For a typical river or a relatively small submarine channel where the effect of Coriolis force can be neglected, no iteration would be required.

3.3. *Complete nonlinear solution*

The complete nonlinear solution is realized as follows. The linear solution is used to estimate the nonlinear residuals and Coriolis terms in the governing equations. These terms act as forcing functions on the linear operators of the remaining terms. The equations can be solved according to appropriate boundary conditions, here taken to be cyclic. The procedure is repeated until convergence is obtained.

The solution at the $(v+1)$th iteration can be obtained from the values of the variables at the vth iteration as follows. Integration of (3.13) in n gives

$$\xi_{dd}^{v+1} = F^2\left[C - f^*(1+u_{dc})^v\right]n + F^2\int_1^n\left(-f^* u_{dd} + R_3\right)^v\mathrm{d}n' + F_{\xi dd}(\phi). \tag{3.29}$$

The free function of integration can be evaluated following the same approach used at the linear level, i.e.

$$F_{\xi dd}(\phi) = \tfrac{1}{2}F^2\int_{-1}^{1}\int_{-1}^{n}(f^* u_{dd} + R_3)^v\,\mathrm{d}n'\,\mathrm{d}n''. \tag{3.30}$$

Integration of (3.11) gives

$$u_{dd}^{v+1} = \mathrm{e}^{-2\phi/r}\left\{u_{dd}|_{\mathrm{u/s}} + \frac{1}{r}\int_0^\phi\left[R_1^v - \bar{R}_1^v - \left(\eta_d - A_s nC + nC + rF^{-2}\frac{\partial \xi_{dd}}{\partial \phi}^{v+1} - \xi_{dd}^{v+1} - f^* v_d^v\right)\right]\mathrm{e}^{2\phi/r}\,\mathrm{d}\phi'\right\}. \tag{3.31}$$

Using the periodic boundary condition, $u_{dd}|_{\mathrm{u/s}}$ can be evaluated as

$$u_{dd}|_{\mathrm{u/s}} = \frac{1}{r(\mathrm{e}^{2\phi_L/r}-1)}\int_0^{\phi_L}\Bigg[R_1^v - \bar{R}_1^v - \left(\eta_d - A_s nC + nC + rF^{-2}\frac{\partial \xi_{dd}}{\partial \phi}^{v+1} - \xi_{dd}^{v+1} - f^* v_d^v\right)\mathrm{e}^{2\phi/r}\,\mathrm{d}\phi\Bigg]. \quad (3.32)$$

Integration of (3.15) in ϕ gives an expression for ξ_{dc}. Depending on whether the flow is supercritical or subcritical, in the Froude sense, i.e. whether $F > 1$ or $F < 1$, the calculation must proceed from upstream or downstream, respectively. If $F > 1$ then

$$\xi_{dc}^{v+1} = \mathrm{e}^{3F_1\phi}\left\{\int_0^{\phi} R_5 \mathrm{e}^{-3F_1\phi}\,\mathrm{d}\,\phi' + \xi_{dc}|_{\mathrm{u/s}}\right\}^v. \quad (3.33)$$

If $F < 1$ then

$$\xi_{dc}^{v+1} = \mathrm{e}^{3F_1\phi}\left\{\xi_{dc}|_{\mathrm{d/s}}\mathrm{e}^{-3F_1\phi_L} - \int_{\phi}^{\phi_L} R_5\,\mathrm{e}^{-3F_1\phi}\,\mathrm{d}\phi'\right\}^v \quad (3.34)$$

where

$$F_1 = \frac{F^2}{r(1-F^2)}. \quad (3.35)$$

The boundary values are determined using periodic conditions and take the following forms for supercritical and subcritical flow, respectively:

$$\xi_{dc}|_{\mathrm{u/s}} = \frac{1}{\mathrm{e}^{3F_1\phi_L}-1}\int_0^{\phi_L} R_5^v \mathrm{e}^{-3F_1\phi}\,\mathrm{d}\phi \quad (3.36)$$

and

$$\xi_{dc}|_{\mathrm{d/s}} = \frac{1}{\mathrm{e}^{-3F_1\phi_L}-1}\int_0^{\phi_L} R_5^v \mathrm{e}^{-3F_1\phi}\,\mathrm{d}\phi. \quad (3.37)$$

From (3.14)

$$u_{dc}^{v+1} = -\left(R_4^v + \xi_{dc}^{v+1}\right) \quad (3.38)$$

and (3.12) can be expressed as

$$v_d^{v+1} = R_2^v - (n+1)r\frac{\partial}{\partial\phi}(u_{dc}+\xi_{dc})^{v+1} - r\frac{\partial}{\partial\phi}\int_{-1}^{n}(u_{dd}+\xi_{dd}-\eta_d)^{v+1}\,\mathrm{d}n'. \quad (3.39)$$

The calculation starts at $v = 1$ with the evaluation of the nonlinear residuals using the known values of the variables from the linear solution. The solution procedure is repeated using the known values on the right-hand sides of (3.29) to (3.39) from the previous or current step until the solution converges to the desired level of accuracy.

In both the linear and nonlinear solutions the gradients of some variables in both the n- and ϕ-directions must be evaluated. In the n-direction a central differencing is used for interior points and a forward and backward differencing is used at $n = -1$ and $n = +1$ respectively. The use of periodic boundary conditions allows central differencing in the ϕ-direction for both interior and end points. If the last node in the calculation domain in streamwise, i.e. ϕ-direction is Imax, then according to the periodic boundary condition,

$$\Gamma_{\text{node Imax+1}} = \Gamma_{\text{node 2}} \quad (3.40)$$

where Γ denotes any variable.

4. Interpretation

4.1. *Interpretation for rivers*

The interpretation of Ikeda, Hino & Kikkawa (1976) of how meanders evolve in subaerial channels is based on the analysis of Engelund (1974). Their treatment focused on the near-bank value of deviatoric streamwise flow velocity u_d. A positive near-bank value of u_d was associated with bank erosion and a negative value with near-bank deposition, so allowing an interpretation of the tendencies for channel shift.

Ikeda *et al.* (1981), Parker *et al.* (1982) and Parker (1983) formalized this interpretation into a quantitative method for predicting channel shift. In particular, the tendency for the streamwise flow velocity to be biased towards one bank or another can be quantified in terms of the locus of high streamwise velocity, as shown in figure 3. The bank toward which the locus is biased is assumed to erode, with the opposite bank depositing so as to maintain constant width as the channel shifts. The locus of high velocity can be quantified in terms of a transverse distance of deviation n_u given by the moment

$$n_u = \frac{\int_{-1}^{1} n(1 + u_{dd} + u_{dc})\,\mathrm{d}n}{\int_{-1}^{1} (1 + u_{dd} + u_{dc})\,\mathrm{d}n}. \tag{4.1}$$

The normal rate of migration of a bank is assumed to depend linearly upon n_u, allowing the channel to shift as shown in figure 3. From (3.23), $u_{dc} = 0$ at the linear level. Combining (3.19) with (A 1), (A 5), and (A 6) it can be readily seen that in the limiting case of very large and small values of r the solution for u_{dd} becomes respectively

$$u_{dd} = -nC \tag{4.2}$$

and

$$u_{dd} = \tfrac{1}{2}\left(A + A_s + F^2 - 1\right) nC. \tag{4.3}$$

It is clear from (4.1), (4.2), and (4.3) that for large and small values of r the thread of high velocity is aligned toward the inner and outer side of the bend respectively. In the first case the meander will die out as the inside of bend is eroded and in the second case the meander will continue to grow as the outside of bend is eroded. In nature most meanders grow in amplitude and they also migrate downstream. The channel selects a value of r (dimensionless wavelength) which pushes the thread of high velocity to the outside of the bend slightly downstream of the apex. Consequently the channel centreline shifts both outward and downstream (Parker 1983). From (A 5) and (A 6), $u_{dd} > 0$ at the outside of a bend apex only if $B_u > 0$. The critical value r_c such that meander amplitude increases for $r < r_c$ is seen from (A 5) to be given as

$$r_c = \sqrt{2[F^2 + A + A_s - 1]}. \tag{4.4}$$

The condition at the linear level for the growth of meander is, therefore, $r_c > r > 0$.

4.2. *Interpretation for subaqueous meandering channels*

Empirical documentation of the mechanism by which meandering develops in channels on subaqueous fans remains sparse and incomplete. It is necessary to understand the nature of their documentation in order to discuss the applicability of the flow

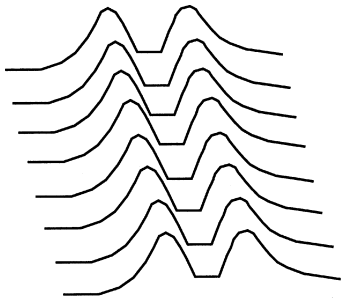

FIGURE 4. Diagram showing the cross-section of an aggrading submarine channel at various times. The diagram illustrates how the channel can shift sideways even though there is net deposition everywhere.

model presented here. Subaqueous fans are essentially depositional environments. The main sources of their documentation are seismic surveys of the seafloor such as those given in Pirmez & Flood (1995). These surveys provide cross-sectional, or in some cases three-dimensional views of the structure of the sedimentary deposits below the seafloor. In such images the channel can often be identified by the 'gull wing' shape denoted in figure 4. A successive stacking of such channels documents channel aggradation as a result of sediment deposition. It is observed in some cases (e.g. Kenyon, Amir & Cramp 1995) that as the channel migrates upward due to sediment deposition, it also migrates laterally. As shown in figure 4, bank erosion is not required in order for lateral migration to occur in this case. The channel can migrate laterally while maintaining constant width if the following two conditions are fulfilled: (*a*) there is less deposition on one bank of a cross-section than the opposite bank and (*b*) the rate of vertical channel aggradation is sufficiently high relative to the rate of bank deposition. Thus channel migration can occur in a purely depositional setting. That the migration of subaqueous meandering channels does occur in purely or predominantly depositional settings is documented by the presence of bend cutoffs on e.g. the channels of the Amazon submarine fan (Damuth *et al.* 1988; Pirmez 1994). Such cutoffs are, however, noticeably less frequent in meandering channels on submarine fans than they are in the case of alluvial rivers. The implication is that lateral shift of aggrading channels on submarine fans may be less dynamic than it is in the case of rivers.

The analysis presented in the previous section can nevertheless be used to obtain at least a qualitative picture of the tendency for meander development in such channels. For example, even in a purely depositional setting, the near-bank value of deviatoric velocity u_d may positive against one bank, so suppressing deposition there, and negative against the opposite bank, so enhancing it. This can lead to channel shift and the increase of channel sinuosity without channel narrowing as long as the bank deposition rate is sufficiently low compared to the vertical aggradation rate. If in turn the vertical aggradation rate is sufficiently small compared to a characteristic response time of the flow, the quasi-steady analysis of flow in meandering channels presented in the previous section allows an interpretation of the tendency for meander amplitude to grow. This interpretation follows that presented for rivers in terms of the locus of high streamwise velocity.

Recently, however, three-dimensional seismic images of buried aggradational submarine channels have suggested that in some cases the channels appear spontaneously with high-amplitude meanders. The channel then aggrades upward without showing

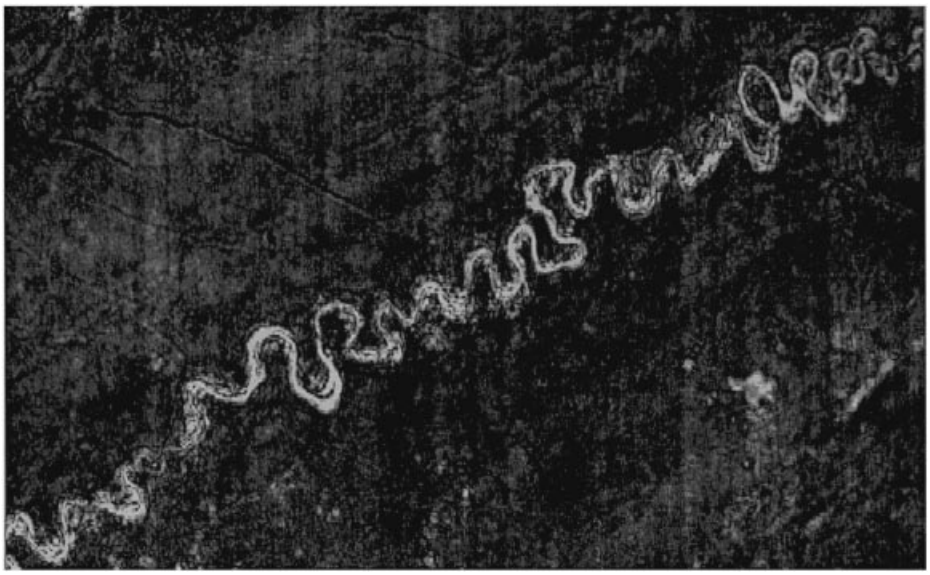

FIGURE 5. Planform of a submarine meandering channel from the subsurface tertiary of West Africa. The three-dimensional seismic image of the channel reach revealed vertical aggradation without much evidence of lateral migration. Courtesy: V. Kolla.

sufficient evidence of bend migration (Kolla *et al.* 1998). An example of the planform of such a channel is shown in figure 5. The shape of the bends in that figure (which apparently includes an incipient cutoff) is highly reminiscent of alluvial bends in rivers, so suggesting an evolutionary process.

It is suggested here that the process in question may be channel narrowing. Pirmez (1994) and Pirmez & Flood (1995) have documented that when channel avulsion occurs on the Amazon submarine fan, the resulting flow out of the breach remains unchannelized for a time. Subsequently levees build so as to gradually confine the main thread of flow, and the construction of an aggradational channel commences. A process by which high-amplitude meanders can be formed by differential narrowing of the levees in the absence of substantial channel aggradation is outlined in figure 6. The present model can be applied at least qualitatively to this case as well. That is, the bank/levee near which the deviatoric velocity u_d is positive narrows less rapidly than the opposite bank, near which u_d is negative, resulting in an amplification in sinuosity over time.

Highly sinuous meanders resulting from this narrowing process have been observed in the subaerial environment. The channels of the Okavango River in the Okavango Delta, Africa provide an example. In this case the agent of channel narrowing is the encroachment of papyrus reeds (Smith *et al.* 1997).

5. Results

5.1. *Linear versus nonlinear solution*

The research on river bend evolution due to Ikeda *et al.* (1981), Parker *et al.* (1982), Parker (1983) and Parker & Andrews (1986) employs the present solution for flow in bends only to the linear level. Indeed, at small curvature a linear solution may be sufficient to understand the physics of flow and meander evolution. As meander bends

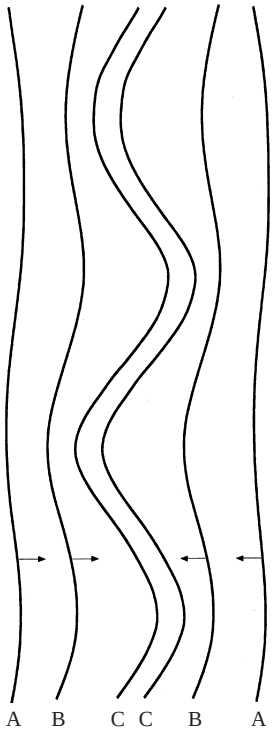

FIGURE 6. Diagram showing channel narrowing process by which a sinuous channel can evolve from an initially wide channel.

continue to grow, however, they evolve into complex shapes with increasingly high curvature, as well as point bars with high amplitude. As curvature and bar amplitude increase nonlinearity in the flow solution can be expected to play an increasing role in the flow dynamics, and thus influence the shape and evolution of meandering. Here the linear, second-order nonlinear and fully nonlinear flow solutions are compared to identify the effects of nonlinearity on the flow field.

5.1.1. *Focus on geometric parameters*

The following base case is used to perform some numerical experiments. The Pembina river in Alberta, Canada represents a fairly typical sand bed stream. A reach of this channel has a width of 80 m, mean bankful depth of 2.5 m, mean velocity of $1.0\,\mathrm{m\,s^{-1}}$, a typical wavelength of 2 km along channel centreline, and a water surface slope of 2.6×10^{-4} (see Johannesson 1988). The above field data give $F = 0.20$, $C_f = 6.4 \times 10^{-3}$, and $r = 1.23$. The sinuosity of the river is around 1.5. An assumed angular amplitude of 72° gives a sinuosity of 1.56. With the above geometric and flow conditions (4.4) indicates that the scour factor A needed for the bend to grow and migrate must be at least 1.72 (neglecting A_s). The typical value of A, however, is around 5 (Johannesson 1988). Figure 7 shows the velocity vectors over one wavelength simulated for the above data with $A = 5.0$. The difference between the linear and fully nonlinear solutions is apparent. Figure 8 shows the linear, second-order nonlinear and fully nonlinear solutions for the variables u_{dd}, v_d, and ξ_{dd} at different sections parallel to the channel centreline (run B of table 1).

Because of its important role in channel shift, the focus of the comparison presented

Run	B/H	F	I	C_f	r	A	θ_0(deg.)	C_0	A_s
B	16.0	0.2	2.6×10^{-4}	6.4×10^{-3}	1.23	5.0	72	0.158	0
A1	16.0	0.2	2.6×10^{-4}	6.4×10^{-3}	1.23	3.0	72	0.158	0
A2	16.0	0.2	2.6×10^{-4}	6.4×10^{-3}	1.23	1.0	72	0.158	0
$\theta 1$	16.0	0.2	2.6×10^{-4}	6.4×10^{-3}	1.43	5.0	60	0.152	0
$\theta 2$	16.0	0.2	2.6×10^{-4}	6.4×10^{-3}	0.91	5.0	90	0.145	0
A_s1	16.0	0.2	2.6×10^{-4}	6.4×10^{-3}	1.23	1.72	72	0.158	0
A_s2	16.0	0.2	2.6×10^{-4}	6.4×10^{-3}	1.23	1.72	72	0.158	1.0

TABLE 1. Input conditions for different numerical runs to find the effect of non-dimensional parameters on the nonlinearity.

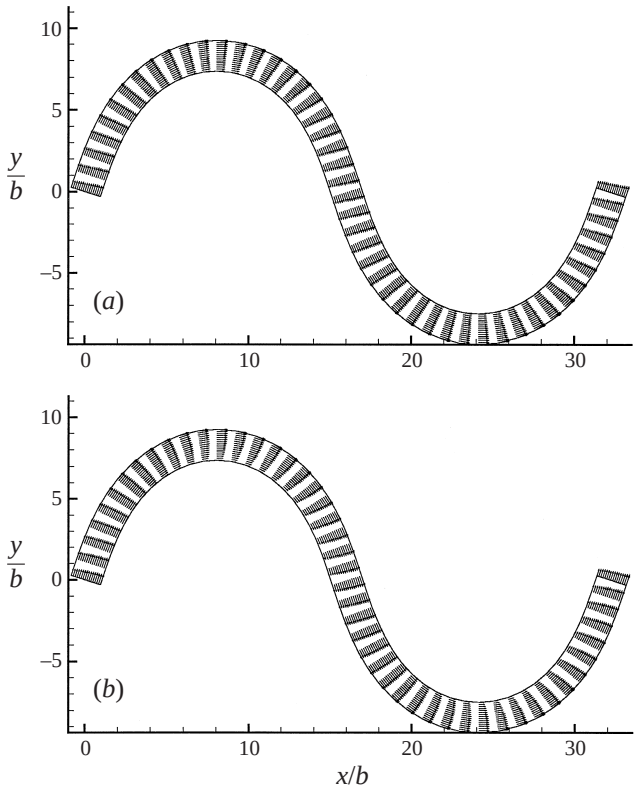

FIGURE 7. Velocity vector at a 72° bend. (*a*) Linear solution; (*b*) nonlinear solution.

below centres on the thread of high velocity. Figure 9 shows the effect of scour factor A on the locus of high velocity. It can be clearly seen that as A increases, the nonlinear solution deviates more from the linear solution. Inputs for figures 9(*a*), 9(*b*), and 9(*c*) are given in rows B, A1, and A2 of table 1 respectively. As expected, it was found that there is no difference between the analytical and numerical solution at the linear level with f set equal to zero.

If r is increased from its base value of 1.23 associated with the example of the Pembina River, θ_0 must be proportionately decreased to maintain the same curvature and, therefore, bed profile. However, changing θ_0 to maintain the same curvature causes the downvalley wavelength to also change in accordance with (3.20).

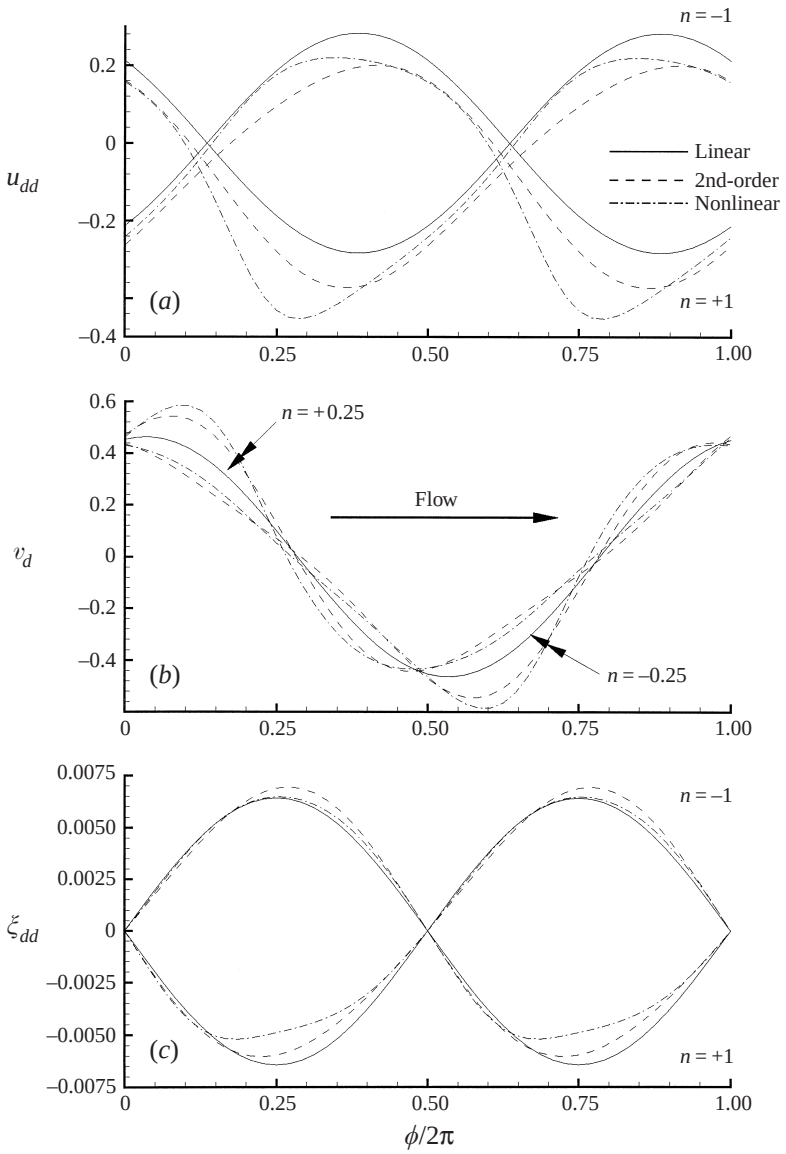

FIGURE 8. Different non-dimensinal flow parameters computed from linear, second-order nonlinear and fully nonlinear solutions for a 72° bend. (*a*) u_{dd} at $n = \pm 1$; (*b*) v_d at $n = \pm 0.25$; (*c*) ξ_{dd} at $n = \pm 1$.

A reasonable compromise would be to study the effect of θ_0 and r together by maintaining a constant downvalley wavelength. In this case, the curvature C_0 would vary only modestly for values of θ_0 ranging between 45° and 90° (figure 10). The combined effect of r and θ_0 for a constant downvalley wavelength is shown in figure 11. For inputs see runs $\theta 1$, B, and $\theta 2$ of table 1. Over this range, changing of θ_0 and r alters the flow only modestly. This is expected because of the constraint according to which r is appropriately changed with θ_0 to maintain a constant downvalley wavelength. In all three cases, however, the differences between the linear, second-order nonlinear and the fully nonlinear solutions are clear. It can be clearly seen

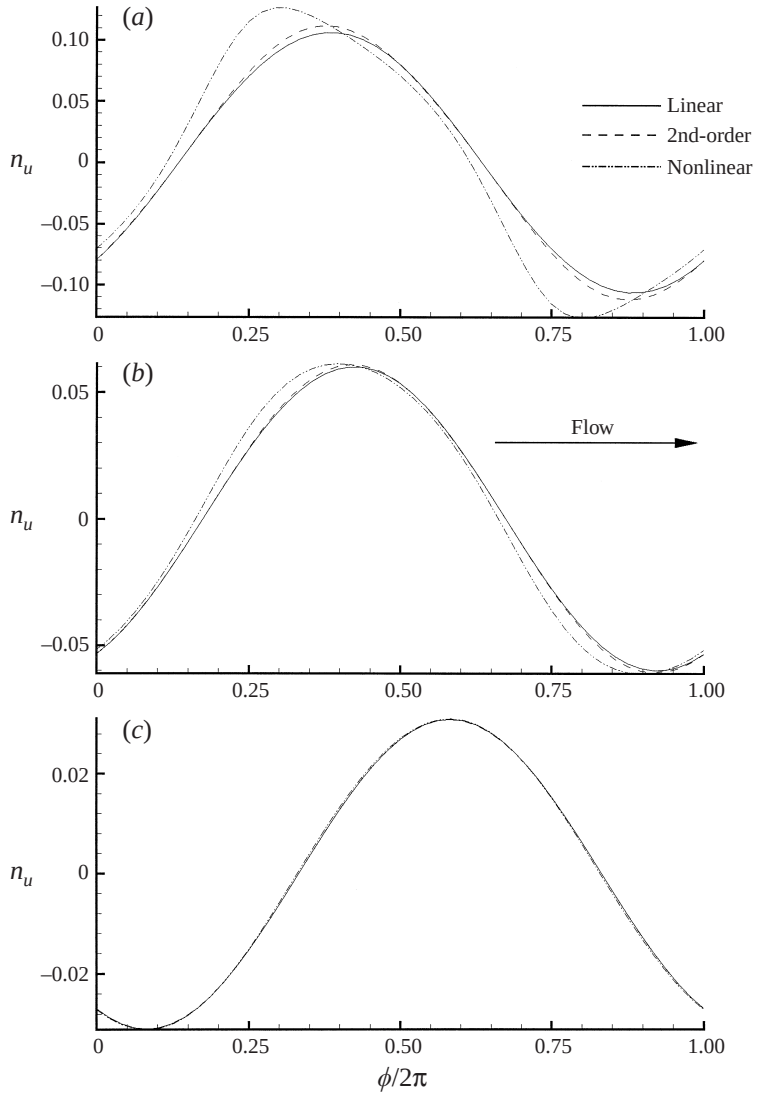

FIGURE 9. Effect of scour factor on the nonlinearity of the flow field. (*a*) $A = 5$; (*b*) $A = 3$; (*c*) $A = 1$.

that n_u obtained from the fully nonlinear solution has a larger maximum value than the linear solution. The differences in magnitude between the linear and second-order nonlinear solutions are relatively small. Even though the normalized curvature is relatively small (around 0.15), the substantial difference between the linear and nonlinear solution is driven by the high lateral bed slope associated with a scour factor of 5.

5.2. *Redistribution of primary flow by the secondary current*

The secondary current redistributes the primary flow momentum and pushes the thread of high velocity towards the outer bank, thus further encouraging the growth of meandering. The importance of this redistribution was described in detail by Johannesson (1988). The role of this redistribution term, which is described by A_s

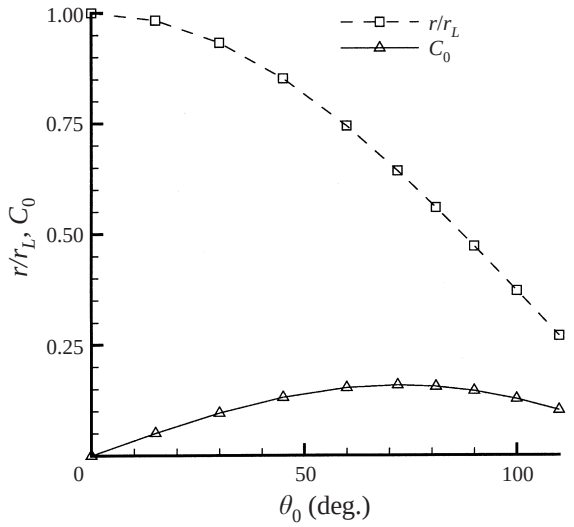

FIGURE 10. Maximum channel centreline curvature C_0 and ratio of linear to arc wavelength (λ_L/λ) for different values of θ_0 but constant λ_L.

in (2.12), is perhaps most evident under conditions that are nearly the critical one for bend growth described by (4.4). The case for the Pembina River described above can be used to clarify this. From the linear theory, the meander bend is at neutral stability when the scour factor has a value of 1.72 and the redistribution term A_s is neglected (run A_s1 of table 1). The value of A_s for this case can be computed to be 1.0 from (2.15). The inclusion of A_s sways the flow toward a condition under which the meander amplitude grows (run A_s2 of table 1). The locus of velocity excess n_u at the nonlinear level for both runs are plotted in figure 12. The difference is clear: in the case $A_s = 0$ it is seen that $n_u = 0$ at the bend apex (maximum C), whereas $n_u > 0$ at the same place if A_s is included.

5.3. *Flow in a meandering submarine channel*

The Amazon Channel, on the submarine fan of the same name, provides a classic example of a strongly meandering submarine channel. Detailed bathymetric data and analysis of the meandering characteristics of the Amazon Fan Channel are available in the literature (Pirmez 1994; Pirmez & Flood 1995). The channel has relatively uniform geometric characteristics (e.g. channel width, depth, wavelength, slope, etc.) in the middle fan region between latitudes of 5° to 7°. Flow is simulated here in a sine-generated curve that approximately represents the characteristics of the Amazon channel in the mid-fan region. The following average values have been estimated from the work of Pirmez (1994): half-width $b = 0.5\,\text{km}$, bankful depth $H = 50\,\text{m}$, linear or downvalley wave length $\lambda_L = 4.5\,\text{km}$, sinuosity (arc wavelength/downvalley wavelength) = 2.0, and a channel slope $I = 2.0\,\text{m km}^{-1}$. Since the channel is dormant during the present high stand of sea, there is no information available on the flow velocity and the concentration of the suspended sediment. Here, a mean reach-averaged velocity of $U = 5.0\,\text{m s}^{-1}$ and a sediment concentration of 2% by volume are arbitrarily assumed, giving a densimetric Froude number of 1.24. These assumed values are reasonable for a submarine turbidity current (Parker *et al.* 1986). Information is not available on lateral bed slope and, therefore, the scour factor A is arbitrarily set equal to zero. A sine-generated curve with an angular amplitude of

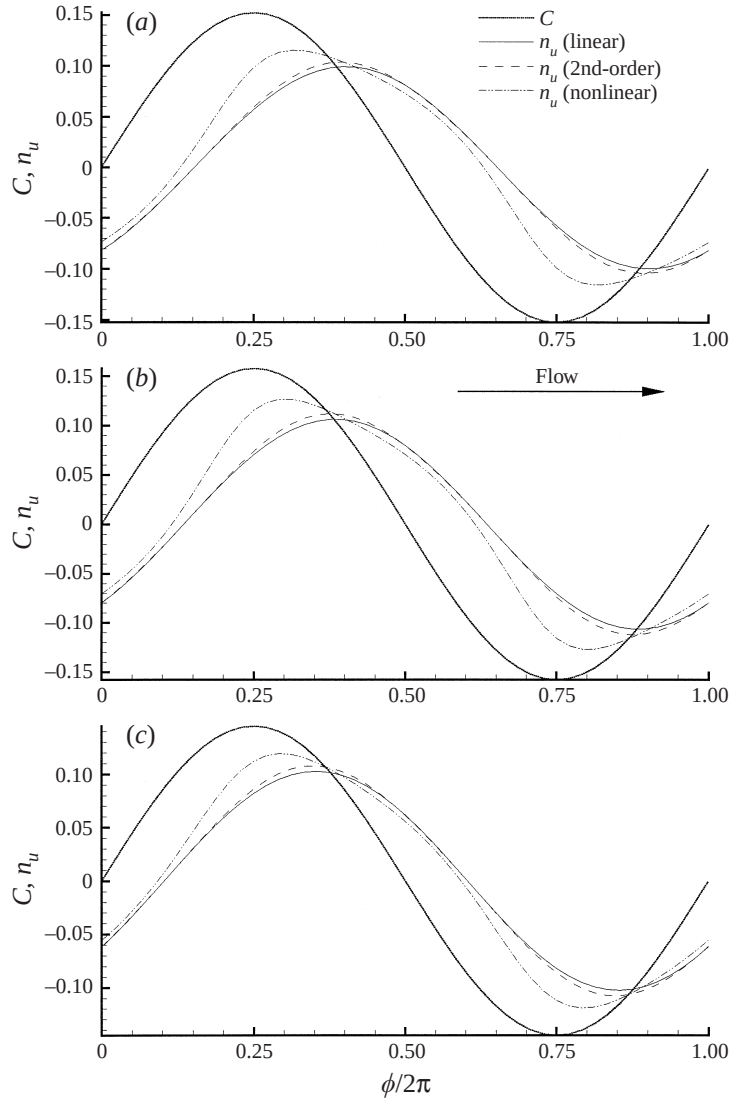

FIGURE 11. Effect of the angular amplitude θ_0 and the normalized wavenumber r on the locus of high velocity. (*a*) $\theta_0 = 60°$, $r = 1.43$; (*b*) $\theta_0 = 72°$, $r = 1.23$; (*c*) $\theta_0 = 90°$, $r = 0.91$.

50° and the above geometric data gives a cross-valley amplitude (distance between two consecutive apexes) of 3.17 km, which is somewhat high but fairly typical of the field data. At a latitude of 6°, the Coriolis force is very small ($f = 1.5 \times 10^{-5}$) and is not expected to play any significant role. The friction factor C_f is estimated from (2.8) under the assumption of base flow condition neglecting the Coriolis force. With the above information, the non-dimensional parameters r and F can be estimated as 26.96 and 1.24, respectively. Applying the same geometric and flow conditions to a river gives $F = 0.226$, and $I = 6.6 \times 10^{-5}$. Even with the same geometry and flow velocity, the Froude number in the subaerial case is approximately 20% of the subaqueous case. At the linear level, it can be easily shown that a submarine channel

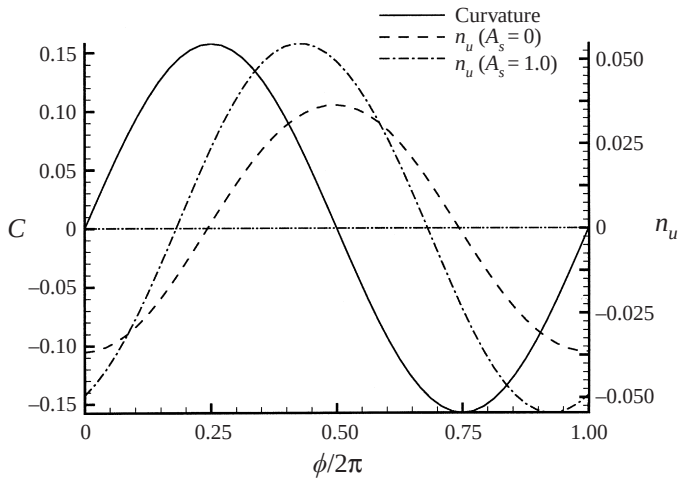

FIGURE 12. The role of redistribution of primary flow momentum by the secondary current in the growth of meander bends. The change in the locus of high velocity can be clearly seen as A_s is considered.

is dynamically equivalent to a river if the following condition is fulfilled:

$$[F^2 + A]_{\text{submarine}} = [F^2 + A]_{\text{subaerial}}. \tag{5.1}$$

Recalling that $A_{\text{submarine}}$ has been set equal to zero, (5.1) yields a scour factor A of 1.49 for the equivalent river. Numerical simulations are performed with the above data (summarized as run SUB1 and RIV1 in table 2) for a submarine and subaerial channel.

Linear and fully nonlinear solutions across two apexes and the crossing (defined in figure 3*a*) are compared in figures 13 and 14. At the linear level (figure 13) u_{dd} and v_d match each other in the two environments due to the imposition of (5.1). However, there is a dramatic difference in the case of ξ_{dd}. The superelevation in the river is more than one order of magnitude smaller than that in the submarine channel. In the case of the fully nonlinear solution (figure 14), the difference between the submarine and subaerial environment in u_{dd} is modest; in v_d it is noticeable and in ξ_{dd} it is again dramatic. In particular, the predicted difference between the height of the flow interface (water surface elevation) at the outside of a bend apex and the inside of the same apex is seen to be over 80% of the mean flow thickness (depth) in the submarine case, but less than 4% in the subaerial case. The extremely large superelevation in the submarine environment can be seen in figure 2 where the surface between a turbidity current and the clear water above shows a dramatic asymmetry associated with a bend.

5.4. *The role of Coriolis force on superelevation of flow thickness*

It is seen from figures 13(*c*) and 14(*c*) that the Coriolis force has almost no effect on the flow at the low latitude of the Amazon Fan. For a larger Coriolis force at a higher latitude, the superelevation would show some asymmetry at the crossing. Since the Coriolis force has been considered by many researchers to be a leading cause of levee asymmetry (Chough & Hesse 1980), its role is studied here by considering the same submarine channel as above but at a higher latitude of 45°, where f is 1.0×10^{-4}. The calculated superelevation of the flow thickness at the crossing (free from the effect of curvature) is shown in figure 15 (run SUB2 of table 2). The effect of the Coriolis force

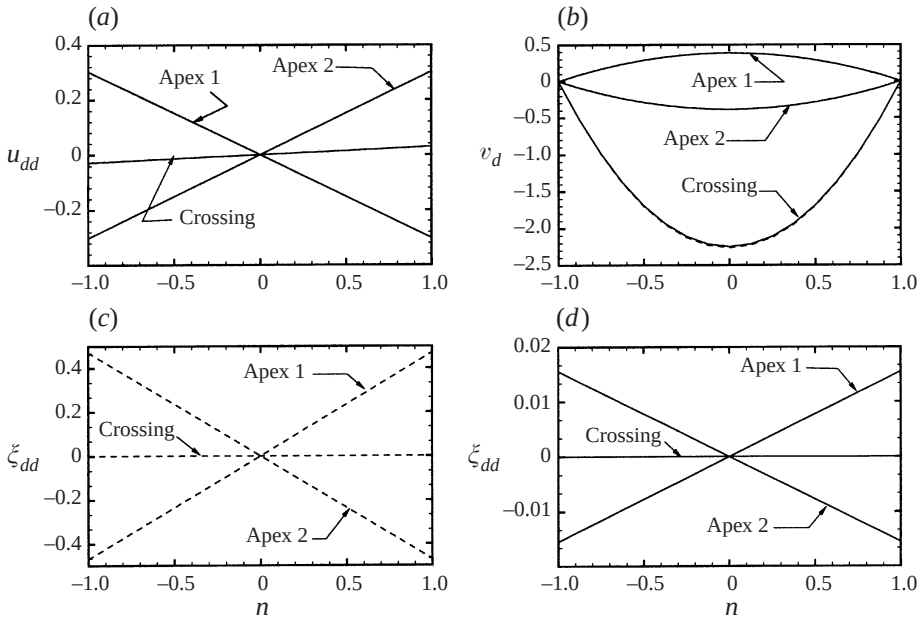

FIGURE 13. Comparison of velocity and superelevation between a submarine channel and equivalent river at the linear level. (*a*) Streamwise velocity excess u_{dd}; (*b*) lateral velocity excess v_d; and (*c*) superelevation ξ_{dd} for submarine channel; (*d*) superelevation ξ_{dd} for river: – – –, submarine; ——, subaerial.

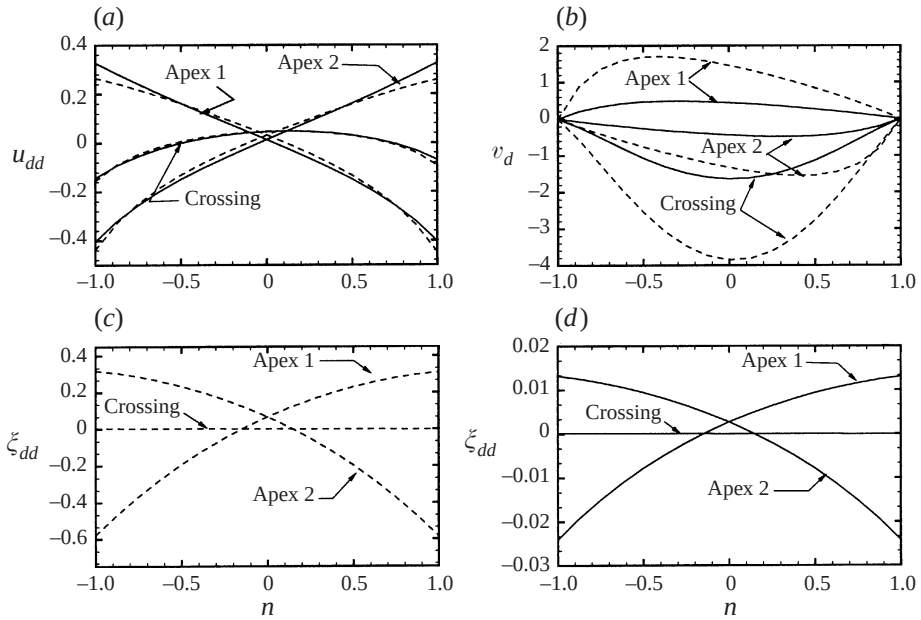

FIGURE 14. Comparison of velocity and superelevation between a submarine channel and equivalent river at the nonlinear level. (*a*) Streamwise velocity excess u_{dd}; (*b*) lateral velocity excess v_d; and (*c*) superelevation ξ_{dd} for submarine channel; (*d*) superelevation ξ_{dd} for river: – – –, submarine; ——, subaerial.

Run	B/H	F	I	C_f	r	A	θ_0(deg.)	C_0	f
SUB1	10.0	1.240	2.0×10^{-2}	12.95×10^{-4}	26.96	0.0	50	0.305	1.5×10^{-5}
RIV1	10.0	0.226	6.6×10^{-5}	12.95×10^{-4}	26.96	1.49	50	0.305	1.5×10^{-5}
SUB2	10.0	1.240	2.0×10^{-2}	12.95×10^{-4}	26.96	0.00	50	0.305	1.0×10^{-4}
RIV2	10.0	0.226	6.6×10^{-5}	12.95×10^{-4}	26.96	1.49	50	0.305	1.0×10^{-4}
SUB3	38.23	1.987	5.0×10^{-4}	25.16×10^{-5}	26.53	0.00	30	0.13	1.0×10^{-4}
SUB4	38.23	1.987	5.0×10^{-4}	25.16×10^{-5}	26.53	0.00	30	0.13	1.5×10^{-5}

TABLE 2. Input conditions for different numerical runs for submarine channels and their subaerial equivalents.

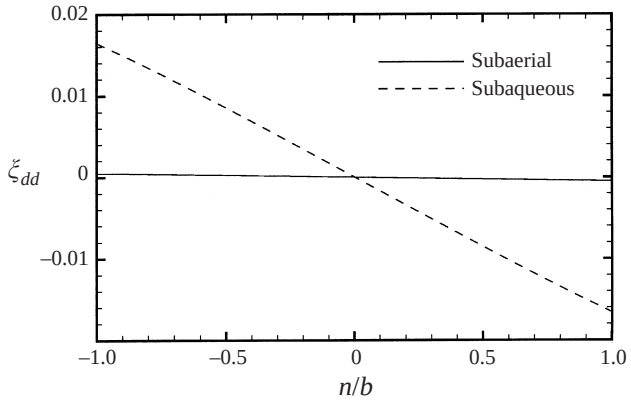

FIGURE 15. Plot of superelevation at the crossing shows the effect of Coriolis force at a higher latitude (45°).

is modest but clearly visible. The elevation difference of the water surface between two banks caused by the Coriolis force at a crossing between bends is about 3% of the flow thickness. For the equivalent river the elevation difference caused by the Coriolis force is well under 0.1% (run RIV2 of table 2). However, comparison of figure 14(*c*) with figure 15 clearly shows that for the length scale (width) of the Amazon Channel even at a higher latitude the effect of channel curvature completely dominates that of the Coriolis force.

This might seem to contradict the observation of strong curvature-independent levee asymmetry observed for the North-West Atlantic Mid-Ocean Channel (NAMOC). In NAMOC, which is only mildly sinuous, the right levee looking downchannel is consistently and substantially higher than the left one (figure 16), a phenomenon which has been attributed to a Coriolis effect so strong that it swamps the effect of curvature (Klaucke, Hesse & Ryan 1998). A consideration of (2.13) in conjunction with the non-dimensionalization of (2.7*d*) allows, however, the inference that the relative effect of the Coriolis force depends on flow scale, and in particular channel width, as well as latitude. In the case of NAMOC, the relative effect of the Coriolis force is amplified compared to the Amazon channel previously considered not only by the high latitude (above 45°) but also a channel width that is an order of magnitude larger.

The present numerical model can be applied to a sine-generated curve that is representative of NAMOC. The following estimates for NAMOC between the latitudes of 44° N and 48° N were extracted from Klaucke *et al.* (1998); half-width

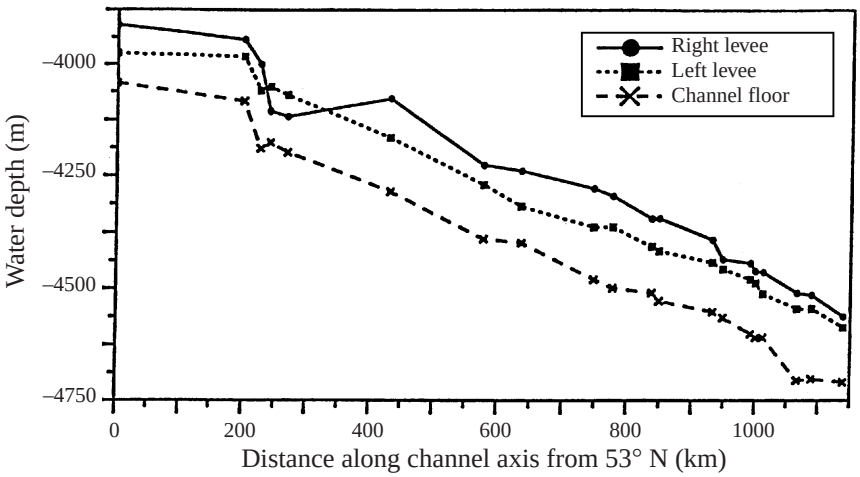

FIGURE 16. Plot of water depth of the NAMOC levees and channel floor showing the consistent asymmetry of levee height (from Klaucke *et al.* 1998).

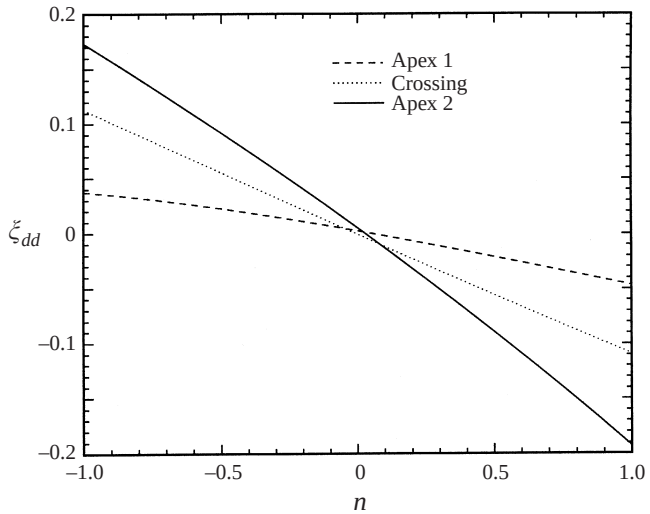

FIGURE 17. Non-dimensional superelevation of flow thickness at two bend apexes and a crossing simulated for the geometry of NAMOC shows that the Coriolis effect is dominant over the centrifugal force.

$b = 6.5$ km, bankful depth, $H = 170$ m, arc wavelength $\lambda = 160$ km, and centreline radius of curvature, $R_c = 50$ km. In addition, Klaucke *et al.* (1998) estimated a velocity of 2.93 m s^{-1} for an excess density of 10 kg m^{-3} which is equivalent to 0.62% by volume. From the above information the input data required to run the model has been determined and listed in table 2 as run SUB3. The simulated superelevation of flow thickness ξ_{dd} at two bend apexes and the crossing are plotted in figure 17. This figure clearly demonstrates that for the geometry, latitude and assumed flow conditons of NAMOC, the Coriolis effect not only dominates mean curvature, but drives a consistent asymmetry in the elevation of the flow interface between the left and right banks that averages to about 22% of mean channel depth. It is of interest to see if the Coriolis force still dominates over the centrifugal force for the geometry

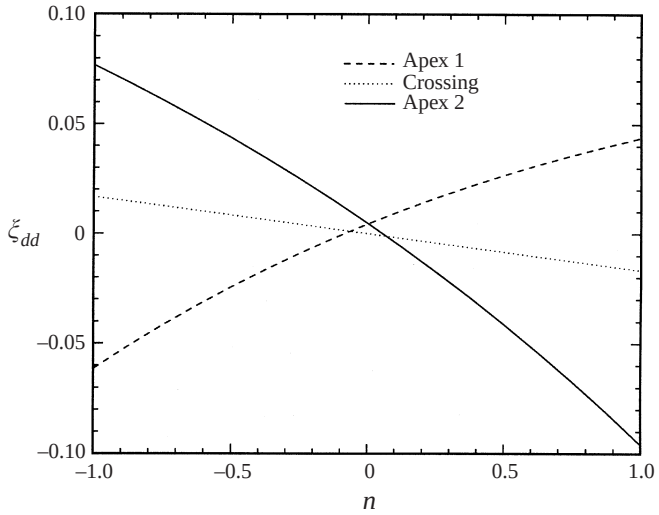

FIGURE 18. Non-dimensional superelevation of flow thickness at two bend apexes and a crossing simulated for the geometry of NAMOC but at a lower latitude of 6° shows a substantially diminished Coriolis effect.

and flow conditions of the NAMOC at a lower latitude of 6° (typical of the Amazon Fan). Figure 18 shows the result of such a calculation with input data listed as SUB4 in table 2. It is found that despite the large scale of the channel the Coriolis effect has diminished at the lower latitude.

5.5. *Search for an appropriate velocity and concentration*

In the analysis of flow in the Amazon Channel, a flow velocity and sediment concentration were assumed such that the flow was mildly supercritical, as is typically assumed in many theoretical and numerical treatments (Parker *et al.* 1986; Imran *et al.* 1998). However, there is no reason to presume that the flow must remain supercritical as it develops far downstream. The flow that has been considered above for the Amazon channel is associated with a normalized wavenumber r that is so high that the meander bends would certainly die in time. That is, $r = 26.96$ for the submarine channel, a value far in excess of the critical value $r_c = 1.04$ calculated from (4.4), below which meander bends increase in amplitude according to the linear theory. The mere existence of a strongly sinuous channel planform indicates that conditions must have existed to encourage the growth of channel meandering. Given the channel geometry it is possible to search for acceptable ranges of flow velocity and sediment concentration that would have allowed the meander bends to grow. From (4.4) the condition at which meander bends are neutrally stable is

$$r^2 = 2(F^2 + A - 1). \tag{5.2}$$

From (5.2) and the definition of F for subaqueous channels given by (2.21), the following expression for concentration c_c at neutral stability can be obtained:

$$c_c = \frac{-2F_2^2 + \sqrt{4F_2^4 + 8J^2F_2^4(A-1)}}{4(A-1)} \tag{5.3}$$

where $J = 2\pi H/\lambda I$ and $F_2 = U(RgH)^{-1/2}$. A necessary condition for meander growth at the linear level is $c < c_c$. For a real solution of (5.3), A must be larger than 1, i.e. the

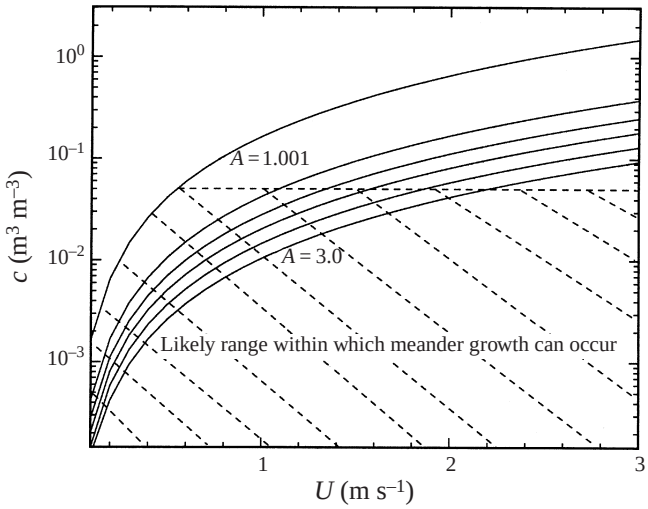

FIGURE 19. Relation between concentration and reach-averaged velocity which is favourable for the growth of submarine meanders.

channel bed must have a finite amount of transverse slope at the bends. This places a lower bound on A in the application of the linear theory to the determination of conditions necessary for the growth of a submarine meandering channel. The linear theory places no intrinsic upper bound on A. That such a bound exists, however, can be seen from (3.21). Let $|\eta_d|_m$ denote the magnitude of the maximum value of $|\eta_d|$ at the banks, i.e. $n = \pm 1$. According to (3.21),

$$|\eta_d|_m = C_0 A. \tag{5.4}$$

If C_0 is infinitesimally small A can be arbitrarily large without making $|\eta_d|_m > 1$, i.e. protruding the bed perturbation above the channel bank. However, for a value of C_0 of 0.305 for the Amazon Channel given in table 2, $|\eta_d|$ exceeds unity for $A > 3.3$. The relationship between c and U is plotted in figure 19 for different values of the scour factor A. In solving (5.3), the following data on the mid-fan region of the Amazon Channel were extracted from Pirmez (1994): $\lambda = 9.0\,\text{km}$, $H = 50\,\text{m}$, and $I = 0.002$. In a turbidity current that can sustain itself over a reasonably long distance, the sediment concentration is likely to be dilute. An upper limit of 5% concentration by volume might be a reasonable approximation. That yields the window for the required velocity range for U and c for subaqueous meander formation for a specific channel as shown in figure 19.

Prediction of the flow field of a turbidity current based on channel geometry is not new. Komar (1969) first used a simple balance between the pressure force, centrifugal force, and the Coriolis force to derive a relationship between flow velocity and sediment concentration. The method was later used by Pirmez (1994) and Klaucke *et al.* (1998) to find flow conditions in the Amazon Channel and the NAMOC respectively. The above mentioned force balance can be expressed as

$$\frac{u^2}{R_c} + fu = Rgc\frac{\Delta\xi}{2b} \tag{5.5}$$

where u is the mean streamwise velocity, R_c is the centreline radius of curvature, $\Delta\xi$ is the elevation difference between two banks, b is the half-width, R is the reduced

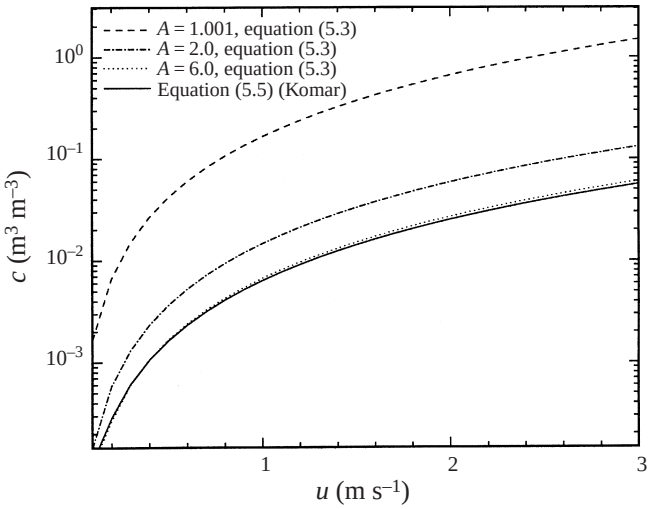

FIGURE 20. Comparison of concentration and reach-averaged velocity calculated from the present linear theory and the force balance relation of Komar (1969).

specific gravity of the suspended sediment, c is the volume concentration of sediment, and f is the Coriolis parameter defined earlier. Note that in (5.5), R_c must be considered to be a parameter that changes sign with changing bend sense in order for the equation to be interpreted correctly. Equation (2.13) of the present analysis can be considered to be a more general form that supersedes (5.5). Although not employed here, another commonly used approach for estimating the flow velocity of a turbidity current is the autosuspension model of Bagnold (1962). Komar (1969) compared concentration and velocity calculated using his force balance equation, i.e. (5.5), and Bagnold's model. Concentration and velocity calculated from the present theory (5.3) and the force balance equation (5.5) of Komar for the above mentioned Amazon Channel are plotted in figure 20. Solution of (5.5) requires some additional information such as asymmetry of levee height and radius of curvature. In the mid-fan region of the Amazon Channel the asymmetry in levee height ΔH is 5 m and the minimum centreline radius of curvature R_c is 1.64 km for the assumed maximum curvature of 0.305. It is found here that the present theory with realistic values of A predicts higher sediment concentration compared to the force balance relation of Komar. If A is increased arbitrarily to a value of 6, the calculations from the two methods show good agreement.

6. Conclusions

A generalized model of flow in meandering submarine and subaerial channels has been presented. The governing equations have been cast in a way which enables their integration without dropping the higher-order nonlinear terms. Solutions obtained at linear and nonlinear levels allow direct comparison between the two. The solution procedure is straightforward and not computationally intensive. Use of the present solution procedure overcomes the limitations associated with a linear model without requiring a significant increase in computational resource or time. The model solves the flow field for depth or current thickness, as well as streamwise and lateral velocity.

Here, the analysis has been focused on the thread of the streamwise velocity excess because it relates the flow field to the channel migration tendencies.

The assumptions made to bring the conservation equations of turbidity currents into the same form as those for open channel flow places some limitations on the application of the model to the submarine environment. In particular, the analysis is not applicable under conditions where the balance between deposition and erosion is far from equilibrium, i.e. the current is either highly depositional or erosional. Such conditions, however, are not conducive to the formation of well-defined meandering channels hundreds of kilometres long such as the Amazon Channel. The analysis provides some insight into the relation between flow in bends and the inception and growth of channel meanders in the submarine environment. The difference in flow thickness between the inner and outer banks has been found to be extremely large in the subaqueous environment. This exaggerated superelevation is supported by an acoustic image of a flow event that took place in a submarine channel in Prince Rupert Inlet, Canada (Hay 1987*b*). The comparison between a submarine and a subaerial channel illustrates both differences and similarities between the two environments. A simple linear analysis yields a range of mean velocities and sediment concentrations that permit the growth of meander bends. The analysis, though, is helpful in constraining the range of flow conditions of turbidity currents which would have formed meandering submarine channels that are dormant in the present geological time.

The present study should be considered a simplified attempt to understand the flow in meandering submarine channels. The limitations placed by considering a conservative developed turbidity current allow comparison between subaerial and submarine environments. In future studies the assumption of a mildly non-conservative turbidity current can overcome this limitation.

We would like to thank Professor Chiang C. Mei and three anonymous reviewers for their valuable suggestions and comments. Funding from the National Science Foundation (Grant No. NSF OCE-9711431 and NSF CTS-9424507) is gratefully acknowledged.

Appendix. First- and second-order analytical solutions for flow in a channel with a sine-generated planform

It is assumed here that the channel planform is given according to the sine-generated curve of equation (3.18), so that the dimensionless channel curvature obeys equation (3.19). In addition, the bed topography is assumed to be given by the simple form of (3.21).

The variables can be expanded in curvature amplitude C_0 (e.g. Johannesson & Parker 1989) as follows:

$$\left.\begin{aligned} u_{dd} &= C_0 u_{dd1} + C_0^2 u_{dd2} + \ldots, \quad \xi_{dd} = C_0 \xi_{dd1} + C_0^2 \xi_{dd2} + \ldots, \\ v_d &= C_0 v_{d1} + C_0^2 v_{d2} + \ldots, \\ \xi_{dc} &= C_0^2 \xi_{dc2} + \ldots, \quad u_{dc} = C_0^2 u_{dc2} + \ldots . \end{aligned}\right\} \tag{A 1}$$

Using the above expansion in (3.11) to (3.13) the following results are obtained at $O(C_0)$:

$$\xi_{dd1} = F^2 n \sin\phi, \tag{A 2}$$

$$r\frac{\partial u_{dd1}}{\partial \phi} + 2u_{dd1} = n\left[(A + A_s + F^2)\sin\phi - r\cos\phi\right] \tag{A 3}$$

and

$$v_{d1} + r\frac{\partial}{\partial\phi}\int_{-1}^{n}\left[u_{dd1} + (F^2 + A)\sin\phi\right] n\,\mathrm{d}n = 0. \tag{A 4}$$

The solution of (A 3) is

$$u_{dd1} = n(A_u\cos\phi + B_u\sin\phi) \tag{A 5}$$

where

$$A_u = -r\frac{A + A_s + F^2 + 1}{4 + r^2}, \quad B_u = \frac{2(A + A_s + F^2 - 1) - r^2}{4 + r^2}. \tag{A 6}$$

Substitution of (A 5) into (A 4) gives

$$v_{d1} + r\frac{\partial}{\partial\phi}\int_{-1}^{n}\left[A_u\cos\phi + B_u\sin\phi + (F^2 + A)\sin\phi\right] n\,\mathrm{d}n = 0 \tag{A 7}$$

which simplifies to

$$v_{d1} = \tfrac{1}{2}r(1 - n^2)\,(A_v\cos\phi - A_u\sin\phi) \tag{A 8}$$

where

$$A_v = (F^2 + A + B_u). \tag{A 9}$$

The following is obtained from (3.13) at $O(C_0^2)$:

$$C_0^2\frac{\partial\xi_{dd2}}{\partial\phi} = R_3 \tag{A 10}$$

where

$$R_3 = C_0^2F^2n[2A_u\sin\phi\cos\phi + (2B_u - 1)\sin^2\phi]. \tag{A 11}$$

The solution of (A 10) is

$$\xi_{dd2} = F^2\left(A_{\xi2} - A_{\xi2}\cos 2\phi + A_u\sin 2\phi\right)\left(\tfrac{1}{2}n^2 - \tfrac{1}{6}\right) \tag{A 12}$$

where

$$A_{\xi2} = B_u - \tfrac{1}{2}. \tag{A 13}$$

Equation (3.11) gives the following at $O(C_0^2)$:

$$C_0^2\left[r\frac{\partial u_{dd2}}{\partial\phi} + 2u_{dd2} - \xi_{dd2} + \frac{r}{F^2}\frac{\partial\xi_{dd2}}{\partial\phi}\right] = R_1 - \bar{R}_1 \tag{A 14}$$

where

$$R_1 = -C_0^2\tfrac{1}{2}\{n^2[(\gamma_1 + \gamma_2) + (\gamma_1 - \gamma_2)\cos 2\phi + \gamma_3\sin 2\phi] + \tfrac{1}{2}r[(\gamma_4 + \gamma_5) + (\gamma_4 - \gamma_5)\cos 2\phi + \gamma_6\sin 2\phi]\} \tag{A 15}$$

and

$$\gamma_1 = A_u^2 + rA_uB_u - \tfrac{1}{2}rA_uA_v, \tag{A 16a}$$

$$\gamma_2 = B_u^2 + A^2 + F^4 - 2AB_u + 2B_u + 2AF^2 - F^2 - A - 2B_uF^2 + \tfrac{1}{2}rA_u - rA_uB_u + \tfrac{1}{2}rA_uB_u, \tag{A 16b}$$

$$\gamma_3 = 2A_uB_u - 2AA_u + 2A_u - 2A_uF^2 - \tfrac{1}{2}rA_v - rA_u^2 + rB_u^2 - \tfrac{1}{2}rA_vB_u + \tfrac{1}{2}rA_u^2, \quad \text{(A 16}c\text{)}$$

$$\gamma_4 = A_uA_v, \quad \gamma_5 = -A_u(1+B_u), \quad \gamma_6 = A_v + A_vB_u - A_u^2, \quad \text{(A 16}d\text{–}f\text{)}$$

and

$$\bar{R}_1 = -C_0^2\tfrac{1}{2}\left[(\tfrac{1}{3}\alpha_1 + \alpha_4) + (\tfrac{1}{3}\alpha_2 + \alpha_5)\cos 2\phi + (\tfrac{1}{3}\alpha_3 + \alpha_6)\sin 2\phi\right] \quad \text{(A 17)}$$

where

$$\alpha_1 = \gamma_1 + \gamma_2, \quad \alpha_2 = \gamma_1 - \gamma_2, \quad \alpha_3 = \gamma_3, \quad \text{(A 18}a\text{–}c\text{)}$$

$$\alpha_4 = \tfrac{1}{2}r(\gamma_4 + \gamma_5), \quad \alpha_5 = \tfrac{1}{2}r(\gamma_4 - \gamma_5), \quad \alpha_6 = \tfrac{1}{2}r\gamma_6 \quad \text{(A 18}d\text{–}f\text{)}$$

leading to

$$R_1 - \bar{R}_1 = C_0^2\left(\tfrac{1}{6} - \tfrac{1}{2}n^2\right)(\alpha_1 + \alpha_2\cos 2\phi + \alpha_3\sin 2\phi). \quad \text{(A 19)}$$

Finally (A 14) becomes

$$r\frac{\partial u_{dd2}}{\partial \phi} + 2u_{dd2} = \left(\tfrac{1}{2}n^2 - \tfrac{1}{6}\right)(\chi_{u2} + \chi_a\cos 2\phi + \chi_b\sin 2\phi) \quad \text{(A 20)}$$

where

$$\chi_{u2} = F^2A_{\xi 2} - \alpha_1, \quad \chi_a = -\left(F^2A_{\xi 2} + \alpha_2 + 2rA_u\right), \quad \chi_b = \left(F^2A_u - \alpha_3 - 2rA_{\xi 2}\right). \quad \text{(A 21}a\text{–}c\text{)}$$

The solution of (A 20) is

$$u_{dd2} = \left[\tfrac{1}{2}\chi_{u2} + A_{u2}\cos 2\phi + B_{u2}\sin 2\phi\right]\left(\tfrac{1}{2}n^2 - \tfrac{1}{6}\right) \quad \text{(A 22)}$$

where

$$A_{u2} = \frac{\chi_a - r\chi_b}{2(1+r^2)}, \quad B_{u2} = \frac{\chi_b + r\chi_a}{2(1+r^2)}. \quad \text{(A 23}a,b\text{)}$$

At second order R_4 from (3.8) and (3.14) has the following expression:

$$R_4 = -C_0^2\frac{1}{2}\int_{-1}^{1} u_{dd1}(F^2 + A)\sin\phi n\,\mathrm{d}n \quad \text{(A 24)}$$

which simplifies to

$$R_4 = -C_0^2(\beta_1 - \beta_1\cos 2\phi + \beta_2\sin 2\phi), \quad \text{(A 25)}$$

$$\beta_1 = \tfrac{1}{6}(A + F^2)B_u, \quad \beta_2 = \tfrac{1}{6}(A + F^2)A_u. \quad \text{(A 26}a,b\text{)}$$

From (3.16) at $O(C_0^2)$

$$R_5 = F^2\left(\bar{R}_1 - 2R_4 - r\frac{\partial R_4}{\partial \phi}\right). \quad \text{(A 27)}$$

Using (A 17) and (A 25), (A 27) becomes

$$R_5 = C_0^2[\chi_c + \chi_d\cos 2\phi + \chi_e\sin 2\phi] \quad \text{(A 28)}$$

where

$$\chi_c = F^2\left(-\tfrac{1}{6}\alpha_1 - \tfrac{1}{2}\alpha_4 + 2\beta_1\right), \quad \chi_d = F^2\left(-\tfrac{1}{6}\alpha_2 - \tfrac{1}{2}\alpha_5, -2\beta_1 + 2r\beta_2\right), \quad \text{(A 29}a,b\text{)}$$

$$\chi_e = F^2\left(-\tfrac{1}{6}\alpha_3 - \tfrac{1}{2}\alpha_6 + 2r\beta_1 + 2\beta_2\right). \quad \text{(A 29}c\text{)}$$

The following is obtained from (3.15):

$$r(1-F^2)\frac{\partial \xi_{dc2}}{\partial \phi} - 3F^2\xi_{dc2} = \frac{R_5}{C_0^2} \tag{A 30}$$

which integrates to

$$\xi_{dc2} = -\frac{\chi_c}{3F^2} + D_{\xi 1}\cos 2\phi + D_{\xi 2}\sin 2\phi \tag{A 31}$$

where

$$D_{\xi 1} = -\frac{3F^2\chi_d + 2r(1-F^2)\chi_e}{9F^4 + 4r^2(1-F^2)^2}, \quad D_{\xi 2} = \frac{\chi_d + 3F^2 D_{\xi_1}}{2r(1-F^2)}. \tag{A 32a,b}$$

The parameter u_{dc2} can be found from the expansion of (3.8) as

$$u_{dc2} = \frac{R_4}{C_0^2} - \xi_{dc2} \tag{A 33}$$

which can be also expressed as

$$u_{dc2} = \left(-\beta_1 + \frac{\chi_c}{3F^2}\right) + \left(\beta_1 - D_{\xi 1}\right)\cos 2\phi - \left(\beta_2 + D_{\xi 2}\right)\sin 2\phi. \tag{A 34}$$

The last unknown v_{d2} can be determined from the expansion of (3.12) at $O(C_0^2)$ leading to

$$v_{d2} + r\frac{\partial}{\partial \phi}\int_{-1}^{n}(u_{dd2} + \xi_{dd2})\,\mathrm{d}n = -\frac{r(n+1)}{C_0^2}\frac{\partial R_4}{\partial \phi} - r(A+F^2) \times \frac{\partial}{\partial \phi}\int_{-1}^{n} u_{dd1}\sin\phi n\,\mathrm{d}n - (1+A)v_{d1}n\sin\phi \tag{A 35}$$

which upon substitution and integration becomes

$$v_{d2} = \left(\chi_f + A_{v2}\cos 2\phi + B_{v2}\sin 2\phi\right)(n - n^3) \tag{A 36}$$

where

$$\chi_f = \tfrac{1}{4}r(1 + A + F^2)A_u, \tag{A 37a}$$

$$A_{v2} = \tfrac{1}{3}r(F^2A_u + B_{u2}) + \tfrac{1}{3}r(A+F^2)A_u - \tfrac{1}{4}r(1+A+F^2)A_u, \tag{A 37b}$$

$$B_{v2} = \tfrac{1}{3}r(F^2A_{\xi 2} - A_{u2}) + \tfrac{1}{3}r(A+F^2)B_u - \tfrac{1}{4}r(1+A+F^2)A_v. \tag{A 37c}$$

REFERENCES

Bagnold, R. A. 1962 Auto-suspension of transported sediment, turbidity currents. *Proc. R. Soc. Lond.* A **265**, 315–319.

Beck, S., Melfi, D. & Yalamanchili, K. 1983 Lateral migration of the Genesee River, New York. In *River Meanders, Proc. ASCE Conf. Rivers*, pp. 510–517.

Blondeaux, P. & Seminara, G. 1985 A unified bar-bend theory of river meanders. *J. Fluid Mech.* **157**, 449–470.

Chough, S. K. & Hesse, R. 1980 The Northwest Atlantic Mid-Ocean Channel of the Labrador Sea: III. Head spill vs. body spill deposits from turbidity currents on natural levees. *J. Sediment. Petrol.* **50**, 0227–0234.

Clark, J. D., Kenyon, N. H. & Pickering, K. T. 1992 Quantitative analysis of the geometry of submarine channels: implications for the classification of submarine fans. *Geology* **20**, 633–636.

Colombini, M., Seminara, G. & Tubino, M. 1987 Finite amplitude alternate bars. *J. Fluid Mech.* **181**, 213–232.

Damuth, J. E., Flood, R. D., Kowsmann, R. O., Belderson, R. H. & Gorini, M. A. 1988 Anatomy and growth pattern of Amazon deep-sea fan as revealed by long-range side-scan sonar (GLORIA) and high resolution seismic studies. *AAPG Bull.* **72**(8), 885–911.

Damuth, J. E., Kolla, V., Flood, R. D., Kowsmann, R. O., Monteiro, M. C., Gorini, M. A., Palma, J. J. C. & Belderson, R. H. 1983 Distributary channel meandering and bifurcation patterns on Amazon deep-sea fan as revealed by long-range side-scan sonar (GLORIA). *Geology* **11**, 94–98.

Droz, L. & Bellaiche, G. 1985 Rhône deep-sea fan: morphostructure and growth pattern. *AAPG Bull.* **69**, 460–479.

Droz, L., Rigaut, F., Cochonat, P. & Tofani, R. 1996 Morphology and recent evolution of the Zaire turbidite system (Gulf of Guinea). *GSA Bull.* **108**, 253–269.

Engelund, F. 1974 Flow and bed topography in channel bends. *J. Hyd. Div. ASCE* **100**, 1631–1648.

Flood, R. D. & Damuth, J. E. 1987 Quantitative characteristics of sinuous distributary channels on the Amazon deep-sea fan. *GSA Bull.* **98**, 728–738.

Garrison, L. E., Kenyon, N. H. & Bouma, A. H. 1982 Channel systems and lobe construction on the Mississippi Fan. *Geo. Mar. Lett.* **2**, 31–39.

Hagen, R. A., Bergersen, D., Moberly, R. & Coulbourn, W. T. 1994 Morphology of a large meandering submarine canyon system the Peru–Chile forearc. *Mar. Geol.* **119**, 7–38.

Hay, A. E. 1987*a* Turbidity currents and submarine channel formation in Rupert Inlet, British Columbia, 1, Surge observations. *J. Geophys. Res.* **92**, 2875–2881.

Hay, A. E. 1987*b* Turbidity currents and submarine channel formation in Rupert Inlet, British Columbia, 2, The roles of continuous and surge type flow. *J. Geophys. Res.* **92**, 2883–2900.

Hickin, E. J. 1974 The development of meanders in natural rivers. *Am. J. Sci.* **274**, 414–442.

Hickin, E. J. & Nanson, G. C. 1975 The character of channel migration on the Beatton River, North East British Columbia, Canada. *GSA Bull.* **86**, 487–494.

Howard, A. D. 1992 Modeling channel migration and floodplain sedimentation in meandering streams. In *Lowland Floodplain Rivers, Geomorphological Perspectives* (ed. P. A. Carling & G. E. Petts), pp. 1–41. John Wiley.

Ikeda, S., Hino, M. & Kikkawa, H. 1976 Theoretical study of the free meandering of rivers. *Proc. Japan Soc. Civil Engng* **255**, 63–73 (in Japanese).

Ikeda, S., Parker, G. & Sawai, K. 1981 Bend theory of river meanders part 1. Linear development. *J. Fluid Mech.* **112**, 363–377.

Imran, J., Parker, G. & Katopodes, N. 1998 A numerical model of channel inception on submarine fans. *J. Geophys. Res.* **103** (C1), 1219–1238.

Johannesson, H. 1985 Computer simulated migration of meandering rivers. MS thesis, University of Minnesota, USA.

Johannesson, H. 1988 Theory of river meanders. PhD thesis, University of Minnesota, USA.

Johannesson, H. & Parker, G. 1989 Linear theory of river meanders. In *River Meandering* (ed. S. Ikeda & G. Parker), pp. 181–213. AGU.

Kenyon, N. H., Amir, A. & Cramp, A. 1995 Geometry of the younger sediment bodies on the Indus Fan. In *Atlas of Deep Water Environments: Architectural Style in Turbidite Systems* (ed. K. T. Pickering, R. N. Hiscott, N. H. Kenyon, F. Ricci Lucci & R. D. A. Smith), pp. 89–93. Chapman and Hall, London.

Kikkawa, H., Ikeda, S. & Kitagawa, S. 1976 Flow and bed topography in curved open channel. *J. Hyd. Div. ASCE* **102**, 1327–1342.

Klaucke, I., Hesse, R. & Ryan, W. B. F. 1998 Morphology and structure of a distal submarine trunk channel: The North-West Atlantic Mid-Ocean Channel between lat 53° N and 44° 30′ N. *GSA Bull.* **110**, 22–34.

Kolla, V., Bourges, P., Urruty, J. M., Claude, D., Morice, M., Durand, E. & Canyon, N. 1998 Reservoir Architecture in Recent and Subsurface, Deep-Water Meandri-Channel and Related Depositional Forms. Extended abstract, 3rd Research Symposium, EAGE/AAPG, Almeira, Spain.

Komar, P. D. 1969 The channelized flow of turbidity currents with application to Monterey deep-sea fan channel. *J. Geophys. Res.* **74**, 4544–4557.

Nelson, J. M. & Smith, J. D. 1989 Evolution and stability of erodible channel beds. In *River Meandering* (ed. S. Ikeda & G. Parker), pp. 321–377. AGU.

Odgaard, A. J. 1981 Transverse bed slope in alluvial channel bends. *J. Hyd. Div. ASCE* **107**(12), 1677–1694.

Parker, G. 1982 Stability of the channel of the Minnesota River near State Bridge no. 93, Minnesota. Project Rep. 205, St. Anthony Falls Laboratory, University of Minnesota, USA.

Parker, G. 1983 Theory of meander bend deformation. *River Meanders, Proc. ASCE Conf. Rivers*, pp. 722–731.

Parker, G. & Andrews, E. D. 1986 On the time development of meander bends. *J. Fluid Mech.* **162**, 139–156.

Parker, G., Diplas, P. & Akiyama, J. 1983 Meander bends of high amplitude. *J. Hydraul. Engng ASCE* **109**, 1323–1337.

Parker, G., Fukushima, Y. & Pantin, H. M. 1986 Self-accelerating turbidity currents. *J. Fluid Mech.* **171**, 145–181.

Parker, G. & Johannesson, H. 1989 Several recent theories of resonance and overdeepening in meandering channels. In *River Meandering* (ed. S. Ikeda & G. Parker), pp. 378–415. AGU.

Parker, G., Sawai, K. & Ikeda, S. 1982 Bend theory of river meanders. Part 2. Nonlinear deformation of finite amplitude bends. *J. Fluid Mech.* **115**, 303–314.

Pirmez, C. 1994 Growth of a submarine meandering channel-levee system on the Amazon Fan. PhD thesis, Columbia University, New York, USA.

Pirmez, C. & Flood, R. D. 1995 Morphology and structure of Amazon Fan Channel. In *Proc. Ocean Drilling Program, Initial Reports*, vol. 155, pp. 23–45.

Salo, J., Kalliola, R., Hakkinen, I., Makinen, Y., Niemela, P., Puhakka, M. & Coley, P. D. 1986 River dynamics and the diversity of Amazon lowland forest. *Nature* **322**, 254–258.

Smith, D. & McLean, S. R. 1984 A model of flow in meandering streams. *Water Resour. Res.* **20**, 1301–1315.

Smith, N. D., McCarthy, T. S., Ellery, W. N., Merry, C. N. & Ruether, H. 1997 Avulsion and anastomosis in the panhandle region of the Okavango Fan, Botswana. *Geomorphology* **20**, 47–65.

Stølum, H. 1996 River meandering as a self-organized process. *Science* **271**, 1710–1713.

Sun, T., Meakin, P. & Jøssang, T. 1996 A simulation model for meandering rivers. *Water Resour. Res.* **32**, 2937–2954.

Tamai, N. & Ikeuchi, K. 1984 Longitudinal and transverse variations of the depth-averaged flow fields in a meandering channel. *J. Hydrosci. Hydraul. Engng* **2**, 11–33.

Weimer, P. 1991 Seismic facies, characteristics, and variations in channel evolution, Mississippi Fan (Plio-Pleistocene), Gulf of Mexico. In *Seismic Facies and Sedimentary Processes of Modern and Ancient Submarine Fans* (ed. P. Weimer & M. H. Link), pp. 323–347. Springer.

Wicker, K. M. 1983 Cutoff bendways and the legal dilemma regarding property ownership. In *River Meandering, Proc. ASCE Conf. Rivers*, pp. 443–452.

Zimmerman, C. & Kennedy, J. F. 1978 Transverse bed slopes in curved alluvial channels. *J. Hydraul. Engng* **104**, 33–48.